Flow Turbulence Combust (2016) 96:1–43
DOI 10.1007/s10494-015-9643-z

A Two-length Scale Turbulence Model for Single-phase Multi-fluid Mixing

J. D. Schwarzkopf[1] · D. Livescu[1] · J. R. Baltzer[1] · R. A. Gore[1] · J. R. Ristorcelli[1]

Received: 23 September 2014 / Accepted: 13 August 2015 / Published online: 8 September 2015
© Springer Science+Business Media Dordrecht 2015

Abstract A two-length scale, second moment turbulence model (Reynolds averaged Navier-Stokes, RANS) is proposed to capture a wide variety of single-phase flows, spanning from incompressible flows with single fluids and mixtures of different density fluids (variable density flows) to flows over shock waves. The two-length scale model was developed to address an inconsistency present in the single-length scale models, e.g. the inability to match both variable density homogeneous Rayleigh-Taylor turbulence and Rayleigh-Taylor induced turbulence, as well as the inability to match both homogeneous shear and free shear flows. The two-length scale model focuses on separating the decay and transport length scales, as the two physical processes are generally different in inhomogeneous turbulence. This allows reasonable comparisons with statistics and spreading rates over such a wide range of turbulent flows using a common set of model coefficients. The specific canonical flows considered for calibrating the model include homogeneous shear, single-phase incompressible shear driven turbulence, variable density homogeneous Rayleigh-Taylor turbulence, Rayleigh-Taylor induced turbulence, and shocked isotropic turbulence. The second moment model shows to compare reasonably well with direct numerical simulations (DNS), experiments, and theory in most cases. The model was then applied to variable density shear layer and shock tube data and shows to be in reasonable agreement with DNS and experiments. The importance of using DNS to calibrate and assess RANS type turbulence models is also highlighted.

Keywords Turbulence · Homogeneous turbulence · Mixing · Variable density · Reynolds stress · Shear · Rayleigh-Taylor · Richtmyer-Meshkov · DNS · Favre average · Compressible flows · Density fluctuations · Two-time scale · Two-length scale · Linear Interaction Approximation · RANS

✉ J. D. Schwarzkopf
jschwar@lanl.gov

[1] Los Alamos National Laboratory, Los Alamos, NM 87545, USA

1 Introduction

The concept of variable density (buoyancy driven) mixing between miscible fluids is well known and is often encountered in practical applications such as ICF, astrophysics, meteorology, and combustion. In these cases, the density variations arise primarily due to compositional changes during mixing of fluids with very different molar masses and from temperature differences. Due to the rapid time scales and small geometries, directly measuring mixing rates within some combustion chambers or the mix that occurs within an ICF capsule poses significant challenges. In general, the flows in such applications are turbulent and may contain multi-physics with sub-continuum phenomena (such as kinetic effects) sometimes bridging with continuum phenomena (e.g. in ICF). The complexity of such problems poses challenges during the development of engineering models; however, aspects of multi-physics flows that occur within these types of applications can be broken into fundamental problems and studied, creating building blocks for engineering models. This allows large-scale, fully resolved simulations of flows in simplified configurations to be used to test, develop, and validate engineering turbulence closures.

Although large-eddy simulation (LES) is increasingly used for modeling turbulent flows, Reynolds (or Favre) averaged Navier-Stokes models still remain useful in simulating mixing effects within complex geometry, multi-physics and multi-scale problems where computational resources prohibit the resolution required for 3D LES. RANS modeling can help a researcher understand the extent of mixing within the practical examples listed above (e.g. ICF) through a 2D axisymmetric simulation, which is much less costly than a full 3D simulation. Even if such 3D simulations were possible, routine simulations for scoping out large portions of a parameter space still require more practical engineering models. Since the target of the RANS model developed here is complex flows of the type encountered in ICF, the model is calibrated to a comprehensive fundamental set of experiments and then applied to a set of experiments that it was not calibrated to.

In recent years, several advancements in engineering models for turbulent mixing in fully compressible and variable density flows have been made. Cebeci and Smith [1] and Besnard et al. [2] introduced Favre average models for turbulence statistics in compressible flows. Besnard et al. [2] introduced the covariance of the specific-volume and density fluctuations, not seen in previous work. Grègoire et al. [3] compared a second moment turbulence model to shock tube data, i.e. the experimental results of Poggi et al. [4] and Andronov et al. [5]. The matching of the turbulence statistics to the data of Poggi et al. was impressive; however, the only comparison to the data of Andronov was the mix width produced by the shocked and re-shocked interface of different density fluids. Grègoire et al. did not assess their model beyond shock driven turbulence. Banerjee et al. [6] discuss a restriction to the work of Besnard et al. [2] for the incompressible case and a simple algebraic expression for the density-specific-volume covariance (denoted hereafter as b) strictly valid for immiscible materials. They applied their models to various mixing problems containing an evolution of a turbulent mixing layer, such as shear and buoyancy driven (or variable density) turbulence, that eventually lead to self-similar growth of a mixing zone. These simple models did show to compare well with the self-similar regimes attained in several experiments and direct numerical simulation (DNS) covering the flows considered, but they had to change the model coefficients from flow to flow to achieve a good match. Stalsberg-Zarling and Gore [7] included a transport equation for b, but they also had to change coefficients for the

flows considered. Schwarzkopf et al. [8] showed that the single-point turbulence equations developed by Besnard et al. [2] could be applied to a range of self-similar turbulent mixing flows generated from different instabilities such as Rayleigh-Taylor, Kelvin-Helmholtz, and Richtmyer-Meshkov without changing the model coefficients. The main reasons for this improvement, compared to Banerjee et al. [6] and Stalsberg-Zarling and Gore [7], were both the introduction of a transport equation for b, instead of ad-hoc algebraic models based on immiscible materials, and full Reynolds stress transport equations. The latter allowed the description of anisotropy, which is important in all unit instability problems considered. However, although the comparisons of turbulence quantities were reasonable, the ability to dial in the growth rates and the magnitudes of the turbulence quantities was difficult. This slight mismatch was related to diffusion and decay models that are slaved to a single term (namely $S = K^{3/2}/\varepsilon$) related to turbulence dissipation, which has a strong influence on both the growth rate of the mixing region and the self-similar turbulence statistics for the different instabilities. In addition, all the above models perform relatively poorly in some basic situations, e.g. a homogeneous version of Rayleigh-Taylor instability. In this case, as explained in Section 5.2, the velocity fluctuations increase initially and then decay in the later stages of the flow, while the density-specific-volume covariance decreases at all times.

Simultaneously matching both the growth rate of the mixing region and the magnitudes, asymmetries, and trends of the turbulence statistics for a variety of turbulence driven instabilities is difficult using conventional averaging techniques. Our proposed effort is to show that a two-length scale model aids in matching both. This type of extension of single-length scale models addresses recent results showing that the transport and dissipation scaling can be very different well after the onset of self-similarity in Rayleigh-Taylor turbulence [9]. The intent of this work is to show that a two-length scale model is capable of capturing both the magnitudes of turbulence statistics and growth rates of the turbulent mixing regions that are generated from various instabilities. Although the focus of the model is directed toward variable density free (unbounded) flows, we have also performed limited comparisons with a wall-bounded flow.

This work differs from shell models (e.g. [10, 11]) where the turbulent energy spectrum is divided into sections that allow a separation of scales (i.e. energy containing and dissipative portions). There have been several studies involving shell models and the application of such models has resulted in good matches to experimental data. Although these models match the experimental data well, they have not been applied to different types of flows that stretch aspects of the model. Multiple time scale approaches, which are a hybrid between a spectral (two-point) model and a single-point model, have been shown to produce better spreading rates than single time scale models for wakes and jets [11].

We hypothesize that the length scale characterizing the turbulent transport should look different than the decay length scale. In current RANS models, such as the k-ε model, the transport term is slaved to the decay length scale (i.e. by coefficients C_μ and σ_k) and as such it cannot capture both homogeneous shear and free shear. The reason can be seen in the profiles across a free shear layer. For example, consider the turbulent kinetic energy transport equation, where the dissipation has a Gaussian shape, peaking at the center of the layer. If the turbulent transport term is slaved to the dissipation using the gradient diffusion hypothesis, then this term becomes a scaled version of the dissipation (i.e. it is also a Gaussian profile). This implies that the transport term will steal away from the production term at the center of the layer and deposit that energy into the edges, helping the growth of the mixing

layer. However, a Gaussian shape for the transport term requires that it steals a lot from the center of the layer and deposits little at the edges, whereas an ideal case would be stealing a little from the center and depositing a lot at the edges. If a separate transport model is used in addition to the dissipation model, then the trends can be separated, which allows more control on the energy deposited at the edges and that transported from the centerline (such as a top-hat profile for the turbulent transport term and Gaussian profile for dissipation). This is the main idea behind the two-length scale approach and why it is different from cascade or spectral models.

The purpose of this paper is fourfold. First, we are interested in highlighting the importance of using DNS to simulate fundamental physics and shed light on strengths and weaknesses of second moment models. Second, we show that a single-length scale model cannot capture the homogeneous and inhomogeneous variants of variable density buoyancy-driven turbulence or shear flow, but the proposed two-length scale model gives better agreement with both. Third, we will show that a simple, single-point, two-length scale model can be extended to a variety of turbulent flows and calibrated to reasonably capture the magnitudes and trends of second moment statistics and the growth rate of a turbulent mixing region along with bridging the gap between homogeneous and free mixing layer flows. The model is calibrated using seven different flows: homogeneous isotropic decaying turbulence, homogeneous buoyancy-driven turbulence (also called homogeneous Rayleigh-Taylor turbulence), homogeneous shear, wall bounded flow, classical Rayleigh-Taylor instability driven turbulence, single-fluid (uniform density) shear driven turbulence, and shocked isotropic turbulence. Finally, we will apply the model to flows that were not used in the calibration and compare to DNS and experimental measurements. While previous models in the class addressed here could, in principle, be calibrated to capture each of these flows separately, this is the first time when such a model shows results that are in reasonable agreement with the DNS and experimental data across a wide variety of buoyancy, shear and shock driven turbulent flows. In addition, this is the first type of RANS model that can begin bridging the homogenous/inhomogeneous gap.

1.1 Motivation

A single-length scale model assumes that the transport length scale is proportional to the cascade (or decay) length scale. If this assumption is valid, then the calibrated second moment Reynolds averaged Navier-Stokes (RANS) equations should capture the differences in turbulent kinetic energy between homogenous and inhomogeneous flows and the growth rate in the latter. However, previous attempts to match both homogeneous shear and mixing layers [8] or homogeneous and classical Rayleigh-Taylor [7] with the same coefficients have been unsuccessful. This suggests that there must be additional physics that distinguish between homogenous and inhomogeneous flows. Studying DNS results showed that not only did the transport and cascade (or decay) length scale need to be separated, but that the production of turbulence mass flux in homogeneous variable density turbulence was over predicted. This introduced the concept of a rapid decay model for the turbulence mass flux equation (originally proposed in [2]), which was not included in [6–8]. In addition, Livescu et al. [9] noted that if the transport length scale was closer to the width of the mixing zone in Rayleigh-Taylor induced turbulence; the growth rate could be better approximated. The idea that transport is associated with a Lagrangian length (or time) scale and the cascade is associated with an Eulerian length (or time) scale is not new. Here we present a simple model that distinguishes the two length scales enough to capture both sets of flows with a single set of coefficients.

2 Recognizing Two Length and Time Scales in Single-point Closures

Historically, turbulent transport has been modeled as a diffusive flux with a diffusion coefficient proportional to a Lagrangian length scale and a Reynolds stress comprised of the Lagrangian covariance, which in homogenous turbulence is approximated by the Reynolds stress covariance of the Eulerian field. The dissipation, on the other hand, has been historically studied using the two point spatial correlation of the Eulerian velocity field.

A short review of the origin of the diffusive model [12, 13] for turbulent transport is useful. For a material conserved scalar, a material property is conserved for a Lagrangian particle. Thus following a Lagrangian particle along its stochastic path from its origin (o) to its final (f) location one conserves the instantaneous quantity c resulting in $c_o = c_f$, where c is a materially conserved quantity. Applying the Reynolds decomposition and expanding the gradient in a Taylor series and retaining only the first terms, one obtains $\bar{c}_o + c'_o = \bar{c}_f + c'_f = \bar{c}_o + \xi_j \bar{c}_{,jo} + c'_f$, where ξ_j is the stochastic location of the Lagrangian fluid particle. If one then takes the moment of the above conservation law with the centered Lagrangian velocity fluctuation at the end of the trajectory $v_k(t_f) = v_{k_f}$, at the origin of the Lagrangian trajectory one has

$$\langle v_k c'_o \rangle = \langle v_k \xi_j \rangle \bar{c}_{,j} + \langle v_k c'_f \rangle, \tag{1}$$

where $\langle\ \rangle$ represents the ensemble average. If the end of the particle trajectory is far enough away to be de-correlated with the initial position, e.g. the diffusion limit where $\langle v_k c'_o \rangle = 0$, one has the gradient transport model

$$\langle v_k c'_f \rangle = -\langle v_k \xi_j \rangle \bar{c}_{,j} = -\int_0^{t_f} \langle v_k(t_f) v_j(t_1) \rangle dt_1 \bar{c}_{,j}, \tag{2}$$

where we have written the final particle position as the temporal integral of the velocity over Lagrangian particle trajectory. The integral in Eq. 2 is written as

$$\langle v_k c' \rangle = -\langle u'_k u'_j \rangle T_L \bar{c}_{,j}, \tag{3}$$

where T_L is the time scale defined by the integral of the Lagrangian two-point correlation between k and j^{th} velocity components and ensemble averaged over the Lagrangian particles. The Lagrangian subscript f is dropped as f is taken to correspond to the local Eulerian position. A simple isotropic model would then result in

$$\langle v_k c' \rangle = -\langle u'_k u'_j \rangle T_L \bar{c}_{,j} = -\frac{C_\mu}{\sigma} k^{1/2} S_T \bar{c}_{,k}, \tag{4}$$

where a transport model for the length scale S_T, as a proxy for the Lagrangian length scale L, e.g. $S_T \approx \frac{2}{3}\frac{\sigma}{C_\mu} L$, is needed. We have used the fact that the Lagrangian velocity at the end of the trajectory, defined by t_f, is the same as the Eulerian velocity at the same spatial location.

There is another length scale and (by suitable normalization) time scale identified and studied in turbulence described as the eddy turnover time and is associated with the inviscid cascade process,

$$\varepsilon = C_\ell \frac{k^{3/2}}{\ell}, \tag{5}$$

which removes energy from the large energy containing scale, at a rate proportional to k/ℓ [14–16]. Mathematically, a length scale based on the two-point correlation of the Eulerian

velocity was identified in early studies of homogenous turbulence, [17, 18] and has been an important direction in turbulence studies [14, 19]. For isotropic turbulence,

$$\ell = \frac{1}{2/3k} \int_0^\infty \langle u'(x)u'(x+r)\rangle dr. \tag{6}$$

This length scale can also be defined as an integral of the energy spectrum and as such bears a relation to the spectrum in a way the Lagrangian time scale and its length scale equivalent, L, does not.

Traditional turbulence models identify the length scale ℓ through the role it plays in the decay of the energy containing scales and then implicitly assume that the flow is self-similar and all length scales are proportional to the eddy turnover length scale ℓ. Our findings show that the inability to capture a number of different flows suggests that a distinction between Lagrangian scales associated with turbulence transport and Eulerian scales associated with the cascade rate may be the key to capture the statistical behavior along with the growth rate of the mixing layer for the variety of flows considered with a single model and set of coefficients. By analogy with Eq. 5, we carry an equation for the length scale defined by the cascade

$$\varepsilon = \frac{k^{3/2}}{S_D}, \tag{7}$$

where S_D is our proxy for the two-point Eulerian integral length scale, similar to S_T being our proxy for the Lagrangian length scale L. We call S_D a decay length scale and distinguish it from S_T the (Lagrangian) transport length scale. The relationship between the length and time scales is then

$$\tau_T = \frac{S_T}{\sqrt{k}}, \text{ and } \tau_D = \frac{S_D}{\sqrt{k}}, \tag{8}$$

where S_T and S_D are turbulent length scales associated with turbulence transport and decay, respectively.

3 Governing Equations

3.1 Instantaneous Equations

The governing equations describing the flow of miscible mixtures of compressible materials are shown below [20, 21]

Continuity:

$$\frac{\partial \rho}{\partial t} + \left(\rho u_j\right)_{,j} = 0\,, \tag{9}$$

Momentum:

$$\frac{\partial \left(\rho u_i\right)}{\partial t} + \left(\rho u_i u_j + P\delta_{ij}\right)_{,j} = \tau_{ij,j} + \rho g_i, \tag{10}$$

Energy:

$$\frac{\partial}{\partial t}\left(\rho E\right) + \left(\rho u_j E + P u_j\right)_{,j} = \left(\tau_{ij}u_i - q_j^c - q_j^d\right)_{,j}, \tag{11}$$

Species Mass Fraction:

$$\frac{\partial\left(\rho c^{n}\right)}{\partial t}+\left(\rho u_{i} c^{n}\right)_{,\,i}=J^{n}_{i,\,i}, \tag{12}$$

where ρ is the material density, u is the fluid velocity, P is the pressure, τ is the viscous stress tensor, g is gravity, E is the total energy, q^{c} is the conductive heat flux, q^{d} is the interdiffusional enthalpy flux, c^{n} is the mass fraction of species n, and J^{n}_{i} is the diffusive mass flux. The above equations should be supplemented with equations of state (pressure and caloric) and expressions for the molecular transport terms: viscous stresses, conduction, enthalpy diffusion, and mass diffusion.

The above equations (9-12) when solved without additional modeling are referred to as DNS. DNS is a high fidelity simulation technique that involves very fine resolutions, using high order non-dissipative methods, to capture turbulence scales down to the viscous/diffusive cut-off scales. In the following section, the above variables are decomposed into an average and a fluctuation and closure models are presented. Unlike DNS, these partial differential equations can be used for engineering problems, where the geometry scales may be large compared to the turbulence scales.

3.2 Favre Averaged Equations

Assuming a statistical description of turbulence, the governing equations are averaged over ensembles of independent realizations. The instantaneous variables in equations (9-12) are decomposed into mean and deviation terms, such as $u_{i}=\bar{u}_{i}+u'_{i}$. Favre averages are then formed from the resultant terms, $\tilde{u}_{i}=\overline{\rho u_{i}}/\bar{\rho}=\bar{u}_{i}+\overline{\rho' u'_{i}}/\bar{\rho}$, $u''_{i}=u'_{i}-\overline{\rho' u'_{i}}/\bar{\rho}$, and $\overline{\rho u''}_{i}=0$. Neglecting the molecular transport terms and applying gradient diffusion for the turbulence mass and energy flux, the averaged equations in the modeled form are:

Momentum:

$$\frac{\partial\left(\rho\tilde{u}_{i}\right)}{\partial t}+\left(\bar{\rho}\tilde{u}_{i}\tilde{u}_{j}+\bar{P}\delta_{ij}+\tilde{\rho}\tilde{R}_{ij}\right)_{ij}=\bar{\rho}g_{i}, \tag{13}$$

Energy:

$$\begin{aligned}\frac{\partial}{\partial t}\left(\bar{\rho}\tilde{E}\right)+\left(\bar{\rho}\tilde{u}_{j}\tilde{E}\right)_{,j}&=-\left(\bar{P}\bar{u}_{j}\right)_{,j}-\left(\bar{\rho}\tilde{u}_{i}\tilde{R}_{ij}\right)_{,j}\\&\quad+C_{\mu}\left[\bar{\rho}S_{T}\sqrt{K}\left(\frac{1}{\sigma_{k}}K_{,j}+\frac{C_{v}}{\mathrm{Pr}_{t}}\tilde{T}_{,j}+\frac{1}{\sigma_{c}}\bar{h}^{n}\tilde{c}^{n}_{,j}\right)\right]_{,j},\end{aligned} \tag{14}$$

Species Mass Fraction:[1]

$$\frac{\partial\left(\bar{\rho}\tilde{c}^{n}\right)}{\partial t}+\left(\bar{\rho}\tilde{u}_{j}\tilde{c}^{n}\right)_{,j}=\frac{C_{\mu}}{\sigma_{c}}\left(\bar{\rho}S_{T}\sqrt{K}\tilde{c}^{n}_{,j}\right)_{,j}, \tag{15}$$

where $\tilde{u}$ is the Favre averaged velocity, $\bar{\rho}$ is the mean density, $\bar{P}$ is the mean pressure, $\tilde{R}_{ij}$ is the Favre averaged Reynolds stress, $\left(\tilde{R}_{ij}=\overline{\rho u''_{i}u''_{j}}/\bar{\rho}\right)$, $\tilde{E}$ is the Favre averaged total energy, S_{T} is the turbulent transport length scale, K is the turbulent kinetic energy $\left(K\equiv\tilde{R}_{ii}/2\right)$, h^{n} is the species (n) enthalpy, $\tilde{c}^{n}$ is the species (n) mass fraction and the turbulent Prandtl number is defined as $\mathrm{Pr}_{t}=C_{v}v_{t}/k_{eff}$, where C_{v} is the constant specific

[1]The conservation of mass is identified when the species equation (15) is summed over all species. A requirement for any turbulence model is that the RHS of Eq. 15 go to zero when this summation takes place.

heat (ideal gas is assumed), v_t is the turbulent viscosity $\left(= C_\mu S_T \sqrt{K}\right)$, and k_{eff} is the effective thermal conductivity. The average specific internal energy is $\tilde{I} = \tilde{E} - \frac{1}{2}\tilde{u}_i\tilde{u}_i - K$; the average temperature is determined from the caloric equation of state $\tilde{I} = C_v\tilde{T}$, and the average pressure of the gaseous mixture is modeled by the ideal-gas equation of state $\bar{P} = (\gamma - 1)\,\bar{\rho}\tilde{I}$, where γ is the ratio of specific heats.

Similar to Reynolds averaging, the Favre average technique introduces additional unclosed terms, e.g. the Reynolds stresses. A set of closure models is needed to complete the system of equations.

3.3 Closure Models

In this section, models are proposed to close the additional turbulence quantities shown in Eqs. 13-15. The exact equations and reasons for the choice of models are described in [2, 8]. The Reynolds stress model is based on the work of Besnard et al. [2] and Schwarzkopf et al. [8] and shown as

$$\begin{aligned}\frac{\partial\left(\bar{\rho}\tilde{R}_{ij}\right)}{\partial t} + \left(\bar{\rho}\tilde{u}_k\tilde{R}_{ij}\right)_{,k} = {} & \overbrace{\left[a_i\bar{P}_{,j} + a_j\bar{P}_{,i}\right] - \bar{\rho}\left[\tilde{R}_{ik}\tilde{u}_{j,k} + \tilde{R}_{jk}\tilde{u}_{i,k}\right]}^{\text{Production}} \\ & + \underbrace{\frac{C_\mu}{\sigma_k}\left(\bar{\rho}S_T\sqrt{K}\tilde{R}_{ij,k}\right)_{,k}}_{\text{Transport}} - \underbrace{C_{r3}\bar{\rho}\frac{\sqrt{K}}{S_D}\left(\tilde{R}_{ij} - \frac{1}{3}\tilde{R}_{kk}\delta_{ij}\right)}_{\text{Return to Isotropy}} \\ & \overbrace{-C_{r1}\left[a_i\bar{P}_{,j} + a_j\bar{P}_{,i}\right] + C_{r2}\bar{\rho}\left[\tilde{R}_{ik}\tilde{u}_{j,k} + \tilde{R}_{jk}\tilde{u}_{i,k}\right]}^{\text{Rapid Distortion}} \\ & \underbrace{- C_{r2}\frac{2}{3}\bar{\rho}\tilde{R}_{mk}\tilde{u}_{m,k}\delta_{ij} + C_{r1}\frac{2}{3}a_k\bar{P}_{,k}\delta_{ij}}_{\text{Rapid Distortion}} \underbrace{- \bar{\rho}\frac{2}{3}\frac{K^{3/2}}{S_D}\delta_{ij}}_{\text{Dissipation}}\end{aligned} \tag{16}$$

where S_D is the turbulent decay length scale, S_T is the turbulent transport length scale and a_i is the mean of the mass-weighted velocity fluctuation $\left(a_i \equiv -\overline{u_i''} = \overline{\rho' u_i'}/\bar{\rho}\right)$. We have chosen the *isotropization of production* (IP) model because it has been used for nearly four decades and applied to a variety of engineering flows showing reasonable results and numerical stability with minimal computational expense. Although more advanced models for pressure strain terms exist, application of these models to a wide variety of distortions, such as shocked flows, is limited. Recently, several advanced models for the pressure strain terms were compared to experimental data of simple contracting and expanding flows [22]. The results show that a good pressure strain model remains to be found, and the IP model (with the correct coefficients) was not misaligned with the more advanced models. In variable density turbulence, the pressure strain is highly coupled to the fluctuating density field and barring the existence of advanced models developed for these flows, we have chosen the simple and importantly robust IP model. Grègoire et al. [3] used the IP model in comparison with shock tube data and showed comparable results. As shown later, the anisotropic stress compares reasonably well with experimental data. The Reynolds stress model in Eq. 16 differs from [2, 6–8] by the separation of the decay and transport length scales.

The turbulent mass flux ($\bar{\rho}a_i$) represents the coupling of density and velocity fluctuations. It only appears in compressible or variable density turbulence and is the dominant

form of advection in buoyancy driven turbulence. An evolution equation for the turbulent mass flux (developed by Besnard et al. [2]) is shown in Eq. 17

$$\frac{\partial\left(\bar{\rho}a_i\right)}{\partial t}+\left(\bar{\rho}\tilde{u}_k a_i\right)_{,k}=\underbrace{b\tilde{P}_{,i}-\tilde{R}_{ik}\bar{\rho}_{,k}-\bar{\rho}a_k\tilde{u}_{i,k}}_{\text{Net Production}}+\underbrace{\bar{\rho}\left(a_k a_i\right)_{,k}}_{\text{Redistribution}} \tag{17}$$
$$+\underbrace{\bar{\rho}\frac{C_\mu}{\sigma_a}\left(S_T\sqrt{K}a_{i,k}\right)_{,k}}_{\text{Transport}}-\underbrace{C_{ap}b\bar{P}_{,i}+C_{au}\bar{\rho}a_k\tilde{u}_{i,k}}_{\text{Rapid Destruction}}-\underbrace{C_{a1}\bar{\rho}\frac{\sqrt{K}}{S_D}a_i}_{\text{Final Destruction}}$$

where $b(=-\overline{\rho'v'})$ is the density-specific-volume covariance. The turbulence mass flux model differs from [2, 6–8] by the separation of the decay and transport length scales. A significant difference between this model and prior variants [6–8] is the addition of rapid decay terms, originally hypothesized by [2]. The net production of turbulence mass flux by the pressure gradient is important in variable density turbulence while the mean dilatation term is important in shocked turbulence.

The density-specific-volume covariance ($b=-\overline{\rho'v'}$) is a measure of how well multiple fluids mix. For a perfect mixture, $b=0$, whereas the upper limit for b is based on the immiscible flow case, which for binary fluids is $b=\alpha_1\alpha_2\left(\rho_1-\rho_2\right)^2/\rho_2\rho_1$, where α_1 and α_2 are the volume fractions. The role of b is to moderate the turbulent mass flux ($\bar{\rho}a_i$) production due to a pressure gradient [9]. The evolution of b (see Besnard et al. [2] and further details shown in [8, 9]) with the two-length scale consideration is given as

$$\frac{\partial\left(\bar{\rho}b\right)}{\partial t}+\left(\bar{\rho}b\tilde{u}_k\right)_{,k}=\underbrace{-2\left(b+1\right)a_k\bar{\rho}_{,k}}_{\text{Production}}+\underbrace{2\bar{\rho}a_k b_{,k}}_{\text{Redistribution}}+\underbrace{\bar{\rho}^2\frac{C_\mu}{\sigma_b}\left(\frac{1}{\bar{\rho}}S_T\sqrt{K}b_{,k}\right)_{,k}}_{\text{Transport}}-\underbrace{C_{b1}\bar{\rho}\frac{\sqrt{K}}{S_D}b}_{\text{Dissipation}} \tag{18}$$

The remaining unclosed terms are the transport and decay length scales S_T and S_D, respectively.

In order to capture these different length scales, S_T and S_D, we hypothesize that the two length scales are different enough to require separate transport equations, yet the physical mechanisms are similar enough such that both scales are driven by the same production and destruction mechanisms. We also assume that the scaling process involves different local inverse turbulence acceleration scales (S/K) and altered coefficients, as shown in Eqs. 19 and 20.

$$\frac{\partial\left(\bar{\rho}S_T\right)}{\partial t}+\left(\bar{\rho}\tilde{u}_j S_T\right)_{,j}=\underbrace{-\frac{S_T}{K}\left(\frac{3}{2}-C_1\right)\bar{\rho}\tilde{R}_{ij}\tilde{u}_{i,j}+\frac{S_T}{K}\left(\frac{3}{2}-C_4\right)a_j\bar{P}_{,j}-\left(\frac{3}{2}-C_2\right)\bar{\rho}\sqrt{K}}_{\text{Net Production}}$$
$$+\underbrace{\frac{C_\mu}{\sigma_s}\left(\bar{\rho}S_T\sqrt{K}S_{T,j}\right)_{,j}}_{\text{Transport}} \tag{19}$$

$$\frac{\partial\left(\bar{\rho}S_D\right)}{\partial t}+\left(\bar{\rho}\tilde{u}_j S_D\right)_{,j} = \underbrace{-\frac{S_D}{K}\left(\frac{3}{2}-C_{1v}\right)\bar{\rho}\tilde{R}_{ij}\tilde{u}_{i,j}+\frac{S_D}{K}\left(\frac{3}{2}-C_{4v}\right)a_j\bar{P}_{,j}-\left(\frac{3}{2}-C_{2v}\right)\bar{\rho}\sqrt{K}}_{\text{Net Production}} + \underbrace{\frac{C_\mu}{\sigma_{2s}}\left(\bar{\rho}S_T\sqrt{K}S_{D,j}\right)_{,j}}_{\text{Transport}} \tag{20}$$

The evolution for the turbulence length scale equations (shown above) can be derived from the definition of S, the turbulence dissipation and kinetic energy equations (the reader is referred to [8] for more details on the derivation).

In summary, the two-length scale model (TLSM) consists of the Favre averaged momentum, energy and mass fraction (13-15), supplemented with models for turbulence quantities, such as the Reynolds stress, turbulence mass flux, and density-specific-volume correlation (16-18) and the two-length scale model (19-20). The coefficients for (13-20) have been calibrated based on the several fundamental flows and are given in Table 1; the values are explained in subsequent sections.

4 Numerical Method

The above model was implemented into a compressible 3D Eulerian hydro-code [23]. The code uses a Godunov scheme to solve the mass, momentum and energy equations while

Table 1 Coefficients for single-phase, single and multi-component flows

Coefficient	Value	Description	Calibrated using
C_{a1}	2.8	Slow decay of mass flux	HRT / RT
C_{ap}	0.1	Rapid decay of turb. mass flux	HRT
C_{au}	0.4	Rapid decay of turb. mass flux	SIT
C_{b1}	1.8	Decay of density-sp. vol	HRT / RT
C_{r1}	0.3	Rapid return to isotropy	HRT / RT
C_{r2}	0.6	Rapid return to isotropy	RDT
C_{r3}	1.8	Slow return to isotropy	Shear
C_1	1.6	Growth rate for *SPT**	Shear
C_4	1.1	Growth rate for *VDT***	RT
C_{1v}	1.3	Rapid growth / decay for *SPT*	Shear
$C_{2v}=C_2$	1.77	Slow growth	HIDT
C_{4v}	1.24	Rapid growth / decay for *VDT*	HRT / RT
σ_s	0.1	Diffusion of turbulence length scale	RT / Shear
σ_{2s}	0.6	Diffusion of turbulence length scale	Wall Coords.
C_μ	0.28	$=\nu_t/\left(S_T\sqrt{K}\right)$	RT

Note: Although the coefficients σ_a, σ_b, σ_c, and σ_k are included in the modeled equations for completeness, the values were set to 1.0 and were therefore omitted from this table.

* *SPT* = single-phase turbulence (uniform density)

** *VDT*= variable density turbulence (single-phase)

equations for the turbulence and mix quantities are solved using traditional finite volume methods. Adaptive mesh refinement (AMR) is also used near the interfaces of materials or shocks, where density, pressure and velocity gradients are the basic criteria for mesh refinement (additional information on AMR can be found in [23] and [24]). The boundary conditions are reflective or symmetric and the domain was sized such that the flow did not reach the boundaries.

The implications of self-similarity are different between shear driven and buoyancy driven turbulence. Thus, for the purpose of model comparisons, self-similarity is considered reached when 1) $\mathrm{d}(R_{11}/(\Delta U)^2)/\mathrm{dt} \sim 0$ for shear driven (SD) flows or 2) $\mathrm{d}b/\mathrm{dt} \sim 0$ for Rayleigh-Taylor (RT) or buoyancy driven mixing and, in addition, the growth or spreading rate parameter reaches a constant value. Besides its importance for model comparisons, reaching self-similarity was also used as a grid convergence criterion.

5 Model Calibration

The turbulence models, shown above, contain several coefficients that need calibration. To calibrate these coefficients, simple flow configurations were used such that most of the terms in the equations could be neglected and the remaining non-zero terms are different for each of the configurations considered. The following configurations were used to calibrate the model:

1) Homogeneous isotropic decaying turbulence,
2) Homogeneous buoyancy-driven / decaying turbulence,
3) Homogeneous shear,
4) Wall bounded flow,
5) Rayleigh-Taylor driven turbulence,
6) Shear driven turbulence,
7) Shocked isotropic turbulence,
8) Rapid distortion theory.

5.1 Homogeneous Isotropic Decaying Turbulence

This is a classic turbulent flow where fluid is passed through a grid structure which generates turbulence which then decays downstream of the mesh. During the decay region of the flow, the turbulence is approximately homogenous and isotropic, resulting in a simplified equation set, shown in Eqs. 21 and 16 which are analogous to $dK/dt = -\varepsilon$ and $d\varepsilon/dt = -C_{\varepsilon 2}\varepsilon^2/K$, where K is the turbulence energy and ε is the turbulence dissipation rate.

Reynolds Stress:

$$\frac{d\tilde{R}_{ij}}{dt} = \underbrace{-C_{r3}\frac{\sqrt{K}}{S_D}\left(\tilde{R}_{ij} - \frac{1}{3}\tilde{R}_{kk}\delta_{ij}\right)}_{\text{Return to Isotropy}} \underbrace{-\frac{2}{3}\frac{K^{3/2}}{S_D}\delta_{ij}}_{\text{Dissipation}} \quad \text{or} \quad \frac{\partial K}{\partial t} = \underbrace{-\frac{K^{3/2}}{S_D}}_{\text{Dissipation}}, \tag{21}$$

Turbulence length scale:

$$\frac{\partial S_D}{\partial t} = \underbrace{-\left(\frac{3}{2} - C_{2v}\right)\sqrt{K}}_{\text{Production}}. \tag{22}$$

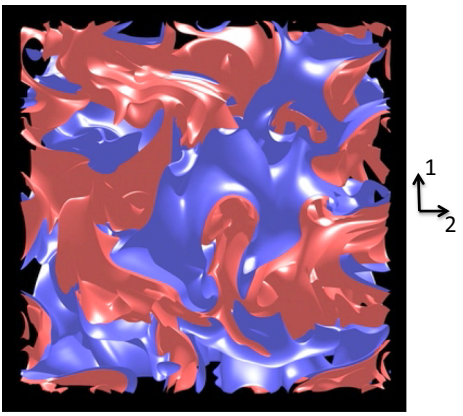

Fig. 1 Initial configuration for the homogeneous Rayleigh-Taylor problem [33–35]. The heavy (blue) and light (red) fluids are initially segregated and turbulence is generated as the fluids start moving in opposite direction due to buoyancy

Hanjalic and Launder [25] used the data of Batchelor and Townsend [26] to determine the model coefficient for the decay of turbulence dissipation. From the data, they deduced that $C_{\varepsilon 2}$ (C_{2v} in this manuscript) must be 2.0. However, Launder, et al. [27] considered an extensive scrutiny of the data which showed that the decay exponent (n, where $K(t) = -K_0(t/t_0)^{-n}$, [19]) should be at least 1.1, which yields a coefficient value 1.9; this value (1.9 or 1.92) is still used in most engineering models [3, 19, 28–30]. However, in 1990, Mohammad and LaRue [31] published additional data on the decay exponent. From their analysis of experimental data over a wide range of mesh Reynolds numbers, the average exponent (n) in the decay model is ~ 1.3, which corresponds to a decay model coefficient of $C_{2v} = 1.77$ [19]. Although reported values for C_{2v} range from 1.4 [32] to upwards of 2.0, we chose to use the value of 1.77, similar to the studies mentioned above. This value was also found to better capture the range of flows discussed here.

5.2 Homogeneous Buoyancy-driven Turbulence

Homogeneous buoyancy-driven turbulence (also referred to as homogenous Rayleigh-Taylor (HRT) turbulence) was first introduced by Sandoval [33] and further studied by Livescu and Ristorcelli [34, 35]. This type of flow initially consists of blobs of miscible fluids having different densities as shown in Fig. 1. At early times, the density-specific-volume covariance is the largest and can be approximated by the two-fluid solution for segregated materials, i.e. $b = \alpha_1\alpha_2 (\rho_1 - \rho_2)^2 / \rho_2\rho_1$ [8], where α_1 and α_2 are the volume fractions associated with the different fluid components in a binary system. A uni-directional body force is then applied and the fluid blobs begin to move and mix. As mixing occurs, the density-specific-volume covariance (b) begins to decay. The presence of the body force creates a mean pressure gradient, which, when coupled to b, produces turbulent mass flux. The coupling between the pressure gradient and the turbulent mass flux generates turbulence energy. As b decreases to zero, the turbulence energy transitions and begins to decay. For the comparisons presented here, we are using a new set of DNS[2], on 1024^3 mesh sizes, covering Atwood numbers, $At = 0.05$, 0.5 and 0.9, defined as $At = (\rho_{high} - \rho_{low})/(\rho_{high} + \rho_{low})$. The turbulence equations (16-18, 20) reduce to ODEs, shown as:

[2]A 1024^3 simulation of this flow at low At has been added to the Johns Hopkins Turbulence databases [36].

Reynolds Stress:

$$\frac{d\tilde{R}_{11}}{dt} = \underbrace{\left(2 - \frac{4}{3}C_{r1}\right)a_1\frac{\bar{P}_{,1}}{\bar{\rho}}}_{\text{Net Production}} - \underbrace{C_{r3}\frac{\sqrt{K}}{S_D}\left(\tilde{R}_{11} - \frac{2}{3}K\right)}_{\text{Return to Isotropy}} - \underbrace{\frac{2}{3}\frac{K^{3/2}}{S_D}}_{\text{Dissipation}} \tag{23}$$

$$\frac{d\tilde{R}_{22}}{dt} = \underbrace{\frac{2}{3}C_{r1}a_1\frac{\bar{P}_{,1}}{\bar{\rho}}}_{\text{Rapid Distortion}} - \underbrace{C_{r3}\frac{\sqrt{K}}{S_D}\left(\tilde{R}_{22} - \frac{2}{3}K\right)}_{\text{Return to Isotropy}} - \underbrace{\frac{2}{3}\frac{K^{3/2}}{S_D}}_{\text{Dissipation}} \tag{24}$$

Turbulence mass flux:

$$\frac{da_1}{dt} = \underbrace{\left(1 - C_{ap}\right)\frac{b}{\bar{\rho}}\bar{P}_{,1}}_{\text{Net Production}} - \underbrace{C_{a1}\frac{\sqrt{K}}{S_D}a_1}_{\text{Destruction}} \tag{25}$$

Density-specific-volume covariance:

$$\frac{db}{dt} = \underbrace{-C_{b1}\frac{\sqrt{K}}{S_D}b}_{\text{Dissipation}} \tag{26}$$

Turbulence length scale:

$$\frac{dS_D}{dt} = \underbrace{\frac{S_D}{\bar{\rho}K}\left(\frac{3}{2} - C_{4v}\right)a_1\bar{P}_{,1} - \left(\frac{3}{2} - C_{2v}\right)\sqrt{K}}_{\text{Net Production}} \tag{27}$$

where the index "1" for tensor quantities denotes the vertical direction, while "2" refers to one of the horizontal directions[3] (Fig. 1).

Contrary to Rayleigh-Taylor instability (RTI) where the turbulence growth becomes self-similar, in this flow it does not. This flow type also exhibits a change in behavior from growth to decay, as the fluids mix, while the density-specific-volume correlation decreases continuously. This turnover in the turbulence energy is very difficult to capture using single-point type models calibrated based on the RTI flow.

It is noted that, while the model reduces to similar b and S equations as the $k-S-a-b$ model of Stalsberg-Zarling and Gore [7] and overall to the same form as the extended model of Schwarzkopf et al. [8], the two-length scale model allows the explicit calibration using the HRT data, unlike the previous models. A comparison of the results of the model described by Stalsberg-Zarling and Gore [7], using a down selection of coefficients, is shown in Fig. 2 along with results using the model and coefficients given by Schwarzkopf et al. [8]. Both calibrations miss the DNS results for $At = 0.25$, although the coefficients suggested by Schwarzkopf et al. [8] show reasonable comparisons for a_{i} and b.[4] For both models [7, 8], the turbulent kinetic energy is off primarily due to a) using the wrong length scale for turbulence dissipation, and b) over predicting the production of the mean mass-weighted velocity fluctuation (a_i).

[3]The average equations corresponding to direction "3" are the same as in the "2" direction.

[4]Note: the coefficients in both models can be changed to exactly match the data set, as Stalsberg-Zarling and Gore [7] showed.

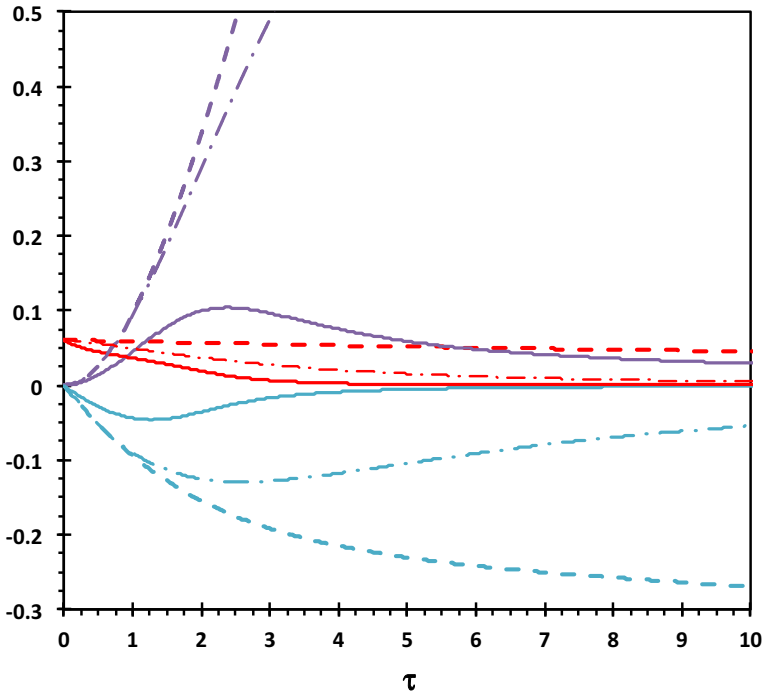

Fig. 2 A comparison of single time scale turbulence models with DNS for HRT, $At = 0.25$ and $\tau = \sqrt{Fr^2/At}$. TKE=purple, b=red, a=cyan; solid lines - DNS, dashed lines - model of Stalsberg-Zarling and Gore [7], dash-dot lines - model of Schwarzkopf et al. [8]

The above ODEs were solved and compared to the DNS results. The variables were initialized with the DNS values at a time that showed the formation of a cascade of turbulence energy from the large scales toward the dissipative scales (based on the Taylor scale Reynolds number, $\mathrm{Re}_\lambda \sim 50$). From the above equations, six coefficients need to be calibrated and although the coefficients can be adjusted to directly match the DNS results, the same coefficients affect Rayleigh-Taylor (RT) driven turbulence and HIDT. The initial value for each coefficient is taken from [8]. The coefficients C_{r1}, C_{ap} and C_{4v} are determined by iterating and comparing results for HRT and RTI, while C_{a1} and C_{b1} were deviated only slightly from the original values given by [8] and C_{r3} remained at 1.8 because a) it affects uniform density shear, and b) Banerjee et al. [22] showed that it compared well with rapid contraction and expansion. The resultant values for the coefficients in Eq. 23-27 are given in Table 1. Comparisons between the model and DNS are shown in Figs. 3, 4 and 5 for $At = 0.05$, 0.5 and 0.9. A comparison of the turbulence statistics shows trends of growth of turbulent kinetic energy which transitions to decay, unlike previous single length scale models, highlighted in Fig. 2. The rapid decay coefficient (C_{ap}) corrects the rising slope of a_i, which also corrects the rising slope of turbulent kinetic energy. Although arguments for the magnitude of the coefficient for homogenous decay (C_{2v}) were made in Section 5.1, this value also affects the decay after the rollover of turbulent kinetic energy (a value of ~1.6 instead of 1.77 would better match the HRT data but obviously does not match homogenous decay).

The magnitudes of the turbulence statistics between the model and DNS are compared over a wide range of At (shown in Figs. 3, 4 and 5). In seeking a better match between the

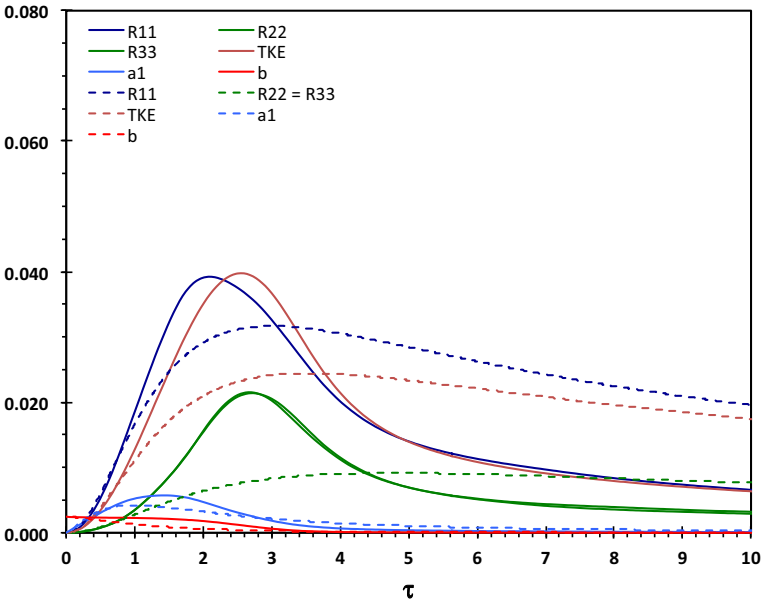

Fig. 3 Comparison of two-length scale model with DNS for $At = 0.05$. Solid lines – DNS, Dashed lines – TLSM

model and simulations, we found discrepancies between the simulation and models for the destruction terms. These discrepancies could be related to the assumption of high Reynolds number turbulence, where destruction terms can be approximated as simple decay models and the dissipation (ε) equation is a scaled version of the kinetic energy (an assumption that is valid when P/ε is quasi-constant). However, for this simple case, the turbulence growth and decay are associated with a strong variation of the turbulence production over dissipation ratio, shown in Fig. 6.

Since the transport length scale does not appear in this flow, Fig. 7 compares the modeled form of the dissipation of turbulence energy, $\varepsilon = K^{3/2}/S_D$, with the exact term $\varepsilon = \overline{\tau'_{ij} u'_{i,j}}$, obtained from DNS. Again, the early time behavior is affected by the large production over dissipation ratio; however, the model reasonably compares with the exact term at higher At.

5.3 Homogeneous Shear

Homogeneous shear is a simple shear flow, where the mean streamwise velocity varies linearly in the cross-stream direction. Studies of homogeneous shear include both experiments [37] and DNS [38]. These two studies show that the flow reaches constant production over dissipation ratio, P/ε,with values of 1.8 and 1.4, respectively. The coefficient C_{1v} can be set using homogeneous shear results. For this flow, the transport terms are zero, and since there are no fluctuations in density, Eqs. 16 and 20 reduce to

$$\frac{dK}{dt} = P - \frac{K^{3/2}}{S_D} \tag{28}$$

$$\frac{dS_D}{dt} = \frac{S_D}{K}\left(\frac{3}{2} - C_{1v}\right) P - \left(\frac{3}{2} - C_{2v}\right)\sqrt{K} \tag{29}$$

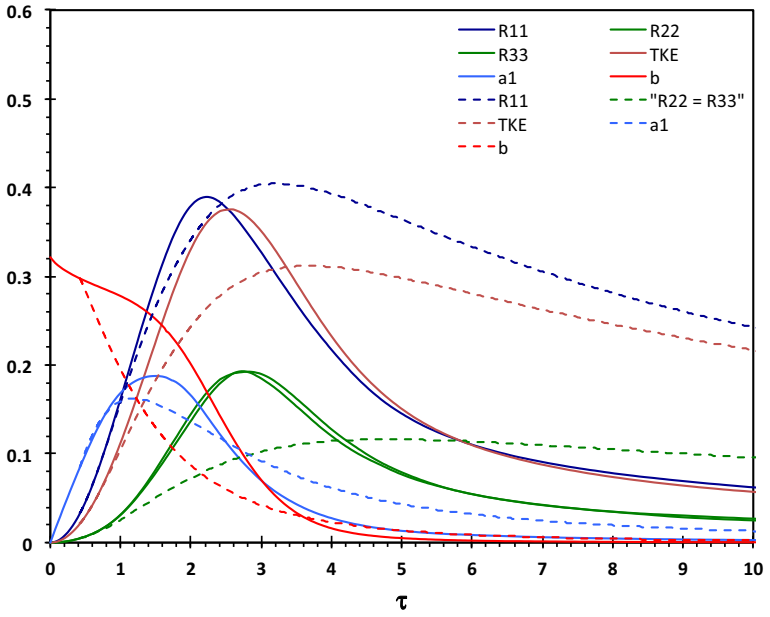

Fig. 4 Comparison of two-length scale model with DNS for $At = 0.5$. Solid lines – DNS, Dashed lines – TLSM

where $\tilde{R}_{ij}$ was contracted to K and P represents the production term.Assuming that the turbulence time scale (K/ε) is constant, then (28) and (29) can be manipulated to give $C_{1v} = 1.0 + \frac{K^{3/2}}{S_D P}(C_{2v} - 1.0)$. Using homogeneous turbulence shear to set C_{1v} introduces errors when extending the equation set to free shear flows where transport is important.[5] Having a coefficient that is dependent solely on ε/P may not be beneficial because if P/ε is the same for both homogeneous and free shear then the computed magnitudes of the Reynolds stress and the growth rate will be less than the measured values. As discussed earlier, the problem stems from the fact that the diffusion model pulls from the center of the mixing layer and distributes at the edges of the region. Matching the Reynolds stress profile of the free shear layer and the growth rate requires $C_{1v} \approx 1.2$ [8], but this value suggests that $P/\varepsilon \sim 3.9$ when applied to homogeneous shear. Schwarzkopf et al. [8] also showed a comparison of the Reynolds stresses using $C_{1v} \approx 1.44$ (satisfying P/$\varepsilon \sim 1.8$) which was ~ 40 % lower than the measured values in free shear and the growth rate was $\sim$ 30 % lower. A reasonable interim solution was found from an iterative approach to obtain $C_{1v} \approx 1.3$, which matches DNS free shear (shown later) and is closer to homogeneous shear $(P/\varepsilon \sim 2.5)$.

5.4 Wall Bounded Flow

Uniform density, single-phase, wall bounded flows are dominated by P/ε balance and driven by shear. While flows of interest in this manuscript do have regions where this is

[5] Including transport in Eq. 28 and the ε-form of Eq. 29 shows that
$C_{1v} = 1.0 + \frac{\varepsilon}{P}(C_{2v} - 1.0) + \frac{T_K - \frac{K}{\varepsilon}T_\varepsilon}{P}$

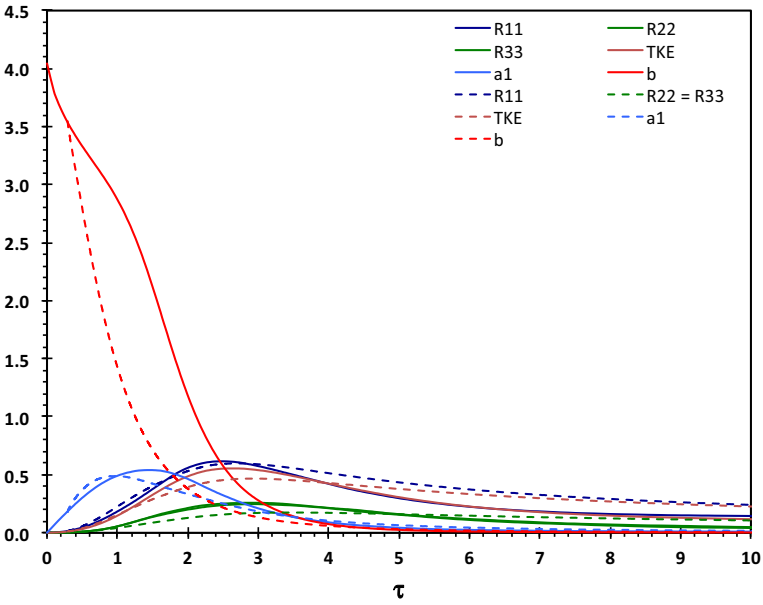

Fig. 5 Comparison of two-length scale model with DNS for $At = 0.9$. Solid lines – DNS, Dashed lines – TLSM

important, there are also regions were the transport to dissipation balance is important. For consistency with literature, we reduce the model to the equation that has been applied to wall flows by removing the equation for S_T and substituting $S_T = S_D$ in the diffusion term of Eq. 20. Assuming that $P = \varepsilon$ and substituting $-\overline{u_1' u_2'} = \tau_w/\rho = U_\tau^2$, $K = U_\tau^2/\sqrt{C_\mu}$ and $S = \kappa y/C_\mu^{0.75}$ into Eq. 20, a relationship between the coefficient values and the von-Kármán constant (κ) can be found, such as $\kappa^2 = \sigma_{2s}\sqrt{C_\mu}\,(C_{2v} - C_{1v})$, which is identical to the expression found from the ε-equation [39]. Banerjee et al. [6] point out that the value for C_μ should be closer to 0.28 for RT, and Chen and Jaw [40] show data that suggest it should be 0.23 for shear driven mixing layers. With the coefficients C_{2v} and C_{1v} set and choosing $C_\mu = 0.28$ an iterative procedure was used between RT, free shear and wall coordinate flows to determine σ_{2s}. Using the suggested coefficient values and $\sigma_{2s} = 0.6$ gives $\kappa \sim 0.39$; which matches well with the range of values of 0.38 to 0.42 obtained in a broad survey of experiments [41].

5.5 Rayleigh-taylor Induced Turbulence

The Rayleigh-Taylor instability forms when a heavy fluid is set above a lighter fluid in the presence of gravity, shown in Fig. 8. The heavy fluid penetrates (spikes) and lighter fluid rises (bubbles) creating a mixing zone. As the spikes and bubbles evolve, turbulence is formed within the mixing zone. Within the turbulent region, the flow is homogeneous in the horizontal directions (i.e. orthogonal to the acceleration), so that the governing equations can be plane averaged and the turbulence quantities become one-dimensional. In this case, index "3" refers to the vertical direction, while "2" is one of the periodic horizontal

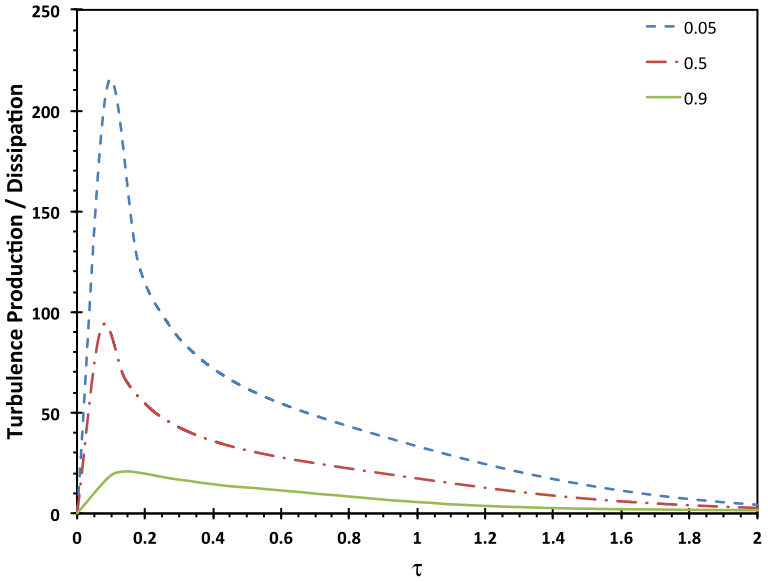

Fig. 6 DNS production / dissipation ratio in HRT at different At, showing large values attained during the growth stage

directions (Fig. 8). The turbulence equations (16-20) and the species mass fraction (15) are reduced for this condition to:

Reynolds Stress:

$$\frac{\partial\left(\bar{\rho}\tilde{R}_{22}\right)}{\partial t}+\left(\bar{\rho}a_3\tilde{R}_{22}\right)_{,3}=\overbrace{\frac{C_\mu}{\sigma_k}\left(\bar{\rho}S_T\sqrt{K}\,\tilde{R}_{22,3}\right)_{,3}}^{\text{Transport}}-\overbrace{C_{r3}\bar{\rho}\frac{\sqrt{K}}{S_D}\left(\tilde{R}_{22}-\frac{2}{3}K\right)}^{\text{Return to Isotropy}}$$
$$\underbrace{-C_{r2}\frac{2}{3}\bar{\rho}\tilde{R}_{33}a_{3,3}+C_{r1}\frac{2}{3}a_3\bar{P}_{,3}}_{\text{Rapid Distortion}}\underbrace{-\bar{\rho}\frac{2}{3}\frac{K^{3/2}}{S_D}}_{\text{Dissipation}} \tag{30}$$

$$\frac{\partial\left(\bar{\rho}\tilde{R}_{33}\right)}{\partial t}+\left(\bar{\rho}a_3\tilde{R}_{33}\right)_{,3}=\overbrace{2\left(1-C_{r1}\right)a_3\bar{P}_{,3}+2\bar{\rho}\left(C_{r2}-1\right)\tilde{R}_{33}a_{3,3}}^{\text{Net Production}}+\overbrace{\frac{C_\mu}{\sigma_k}\left(\bar{\rho}S_T\sqrt{K}\,\tilde{R}_{33,3}\right)_{,3}}^{\text{Transport}}$$
$$\underbrace{-C_{r2}\frac{2}{3}\bar{\rho}\tilde{R}_{33}a_{3,3}+C_{r1}\frac{2}{3}a_3\bar{P}_{,3}}_{\text{Rapid Distortion}}\underbrace{-C_{r3}\bar{\rho}\frac{\sqrt{K}}{S_D}\left(\tilde{R}_{33}-\frac{2}{3}K\right)}_{\text{Return to Isotropy}}\underbrace{-\bar{\rho}\frac{2}{3}\frac{K^{3/2}}{S_D}}_{\text{Dissipation}} \tag{31}$$

Turbulence mass flux:

$$\frac{\partial\left(\bar{\rho}a_3\right)}{\partial t}=\underbrace{\left(1-C_{ap}\right)b\bar{P}_{,3}-\left(\tilde{R}_{33}+a_3a_3\right)\bar{\rho}_{,3}}_{\text{Net Production}}+\underbrace{\bar{\rho}\frac{C_\mu}{\sigma_a}\left(S_T\sqrt{K}a_{3,3}\right)_{,3}}_{\text{Transport}}\underbrace{-C_{a1}\bar{\rho}\frac{\sqrt{K}}{S_D}a_3}_{\text{Destruction}} \tag{32}$$

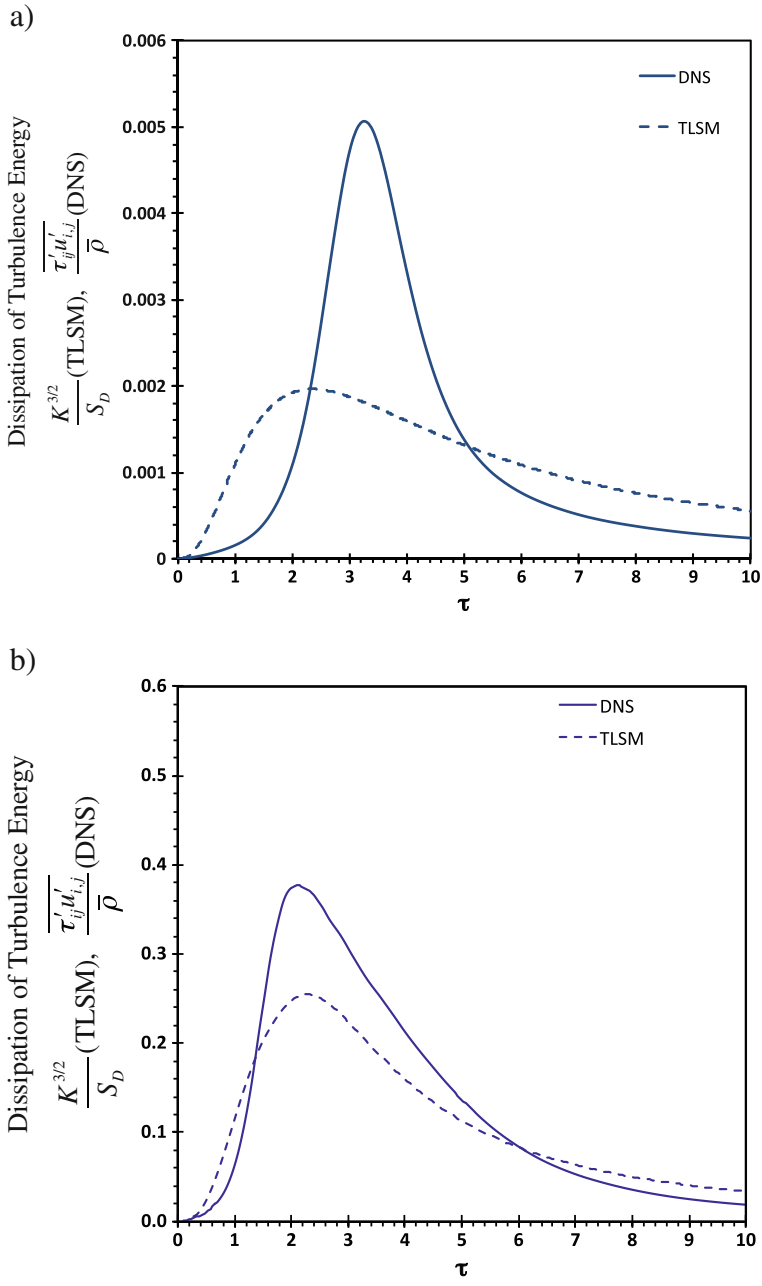

Fig. 7 Comparison of the dissipation of turbulence energy for $At = 0.05$ a) and 0.9 b)

Density-specific-volume covariance:

$$\frac{\partial(\bar{\rho}b)}{\partial t} + (\bar{\rho}a_3 b)_{,3} = \underbrace{2\bar{\rho}a_3 b_{,3} - 2(b+1)a_3\bar{\rho}_{,3}}_{\text{Net Production}} + \underbrace{\bar{\rho}^2\frac{C_\mu}{\sigma_b}\left(\frac{1}{\bar{\rho}}S_T\sqrt{K}b_{,3}\right)_{,3}}_{\text{Transport}} - \underbrace{C_{b1}\bar{\rho}\frac{\sqrt{K}}{S_D}b}_{\text{Dissipation}} \quad (33)$$

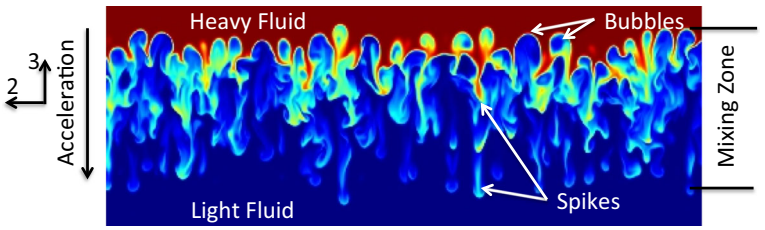

Fig. 8 Early time DNS of the Rayleigh-Taylor instability showing the mixing zone, bubbles and spikes

Turbulence length scale:

$$\frac{\partial\left(\bar{\rho}S_T\right)}{\partial t}+\left(\bar{\rho}a_3S_T\right)_{,3}=\underbrace{\frac{S_T}{K}\left(\frac{3}{2}-C_4\right)a_3\tilde{P}_{,3}-\left(\frac{3}{2}-C_2\right)\bar{\rho}\sqrt{K}}_{\text{Net Production}}+\underbrace{\frac{C_\mu}{\sigma_s}\left(\bar{\rho}S_T\sqrt{K}S_{T,3}\right)_{,3}}_{\text{Transport}} \tag{34}$$

$$\frac{\partial\left(\bar{\rho}S_D\right)}{\partial t}+\left(\bar{\rho}a_3S_D\right)_{,3}=\underbrace{\frac{S_D}{K}\left(\frac{3}{2}-C_{4v}\right)a_3\tilde{P}_{,3}-\left(\frac{3}{2}-C_{2v}\right)\bar{\rho}\sqrt{K}}_{\text{Net Production}}+\underbrace{\frac{C_\mu}{\sigma_{2s}}\left(\bar{\rho}S_T\sqrt{K}S_{D,3}\right)_{,3}}_{\text{Transport}} \tag{35}$$

Species Concentration:

$$\frac{\partial\left(\bar{\rho}\tilde{c}^n\right)}{\partial t}+\left(\bar{\rho}a_3\tilde{c}^n\right)_{,3}=\underbrace{\frac{C_\mu}{\sigma_c}\left(\bar{\rho}S_T\sqrt{K}\tilde{c}^n_{,3}\right)_{,3}}_{\text{Transport}} \tag{36}$$

A comparison of equations (30-36) to the HRT equations (23-27) shows that the main differences are in the advection, diffusion and redistribution terms. Therefore, a turbulence model calibrated to buoyancy driven turbulence must be able to capture both HRT and RT driven turbulence. Schwarzkopf et al. [8] did not use HRT in their calibration, and although not discussed, they found that both the growth rate and the dimensionless magnitudes could not be matched simultaneously for RT. One approach to resolving this inconsistency is by using different turbulent length scales for decay and transport.

The Rayleigh-Taylor (DNS) results of Cabot and Cook [42] analyzed by Livescu et al. [9] at moderate At were used to evaluate the model coefficients for turbulence diffusion. In order to compare the model with DNS, the non-dimensionalization procedure outlined in [8] was used. The length scales were non-dimensionalized by the mixing layer width, $h(t)=6\int_{-\infty}^{\infty}f_v\left(1-f_v\right)dz$, where f_v is the volume fraction, and the velocity scales by $\lambda=\sqrt{h\left(t\right)At\left|g\right|}$, where g is gravitational acceleration. Using these scales, the turbulent kinetic energy and turbulent mass flux can be collapsed and the value and trends have been shown to be independent of temporal and spatial growth (see [8] for further discussion).

For buoyancy induced turbulence (RT), the turbulent kinetic energy and turbulence length scales were initialized with small but non-zero values that were constant across the domain. The turbulent kinetic energy was isotropically distributed across the diagonal components of the Reynolds stress tensor while the off-diagonal components were initialized to zero. The turbulent mass flux was initialized as zero across the domain and the density-specific-volume covariance was initialized as the two-fluid value in the cells adjacent to the interface

of the fluids and zero everywhere else. Since the code is compressible, the temperature was increased to suppress shock formations.

Several coefficients associated with the buoyancy driven variable density turbulence are set within the self-similar growth of a turbulent RT mixing layer. The turbulent Schmidt

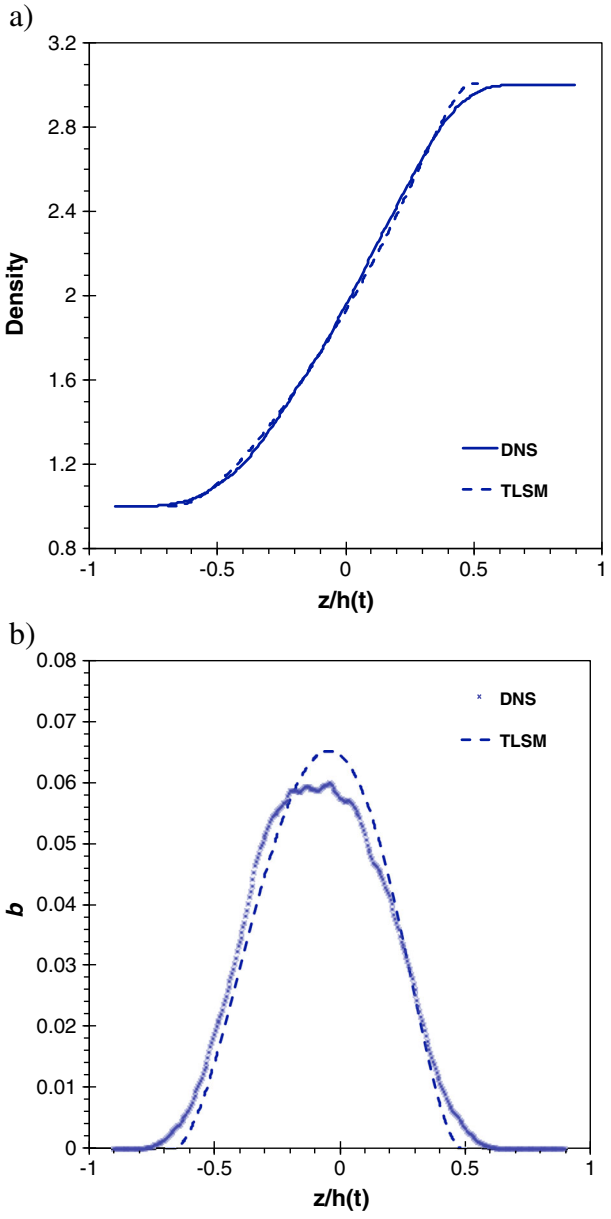

Fig. 9 Direct comparison of the TLSM and DNS for a) density and b) the density-specific volume covariance for $At = 0.5$

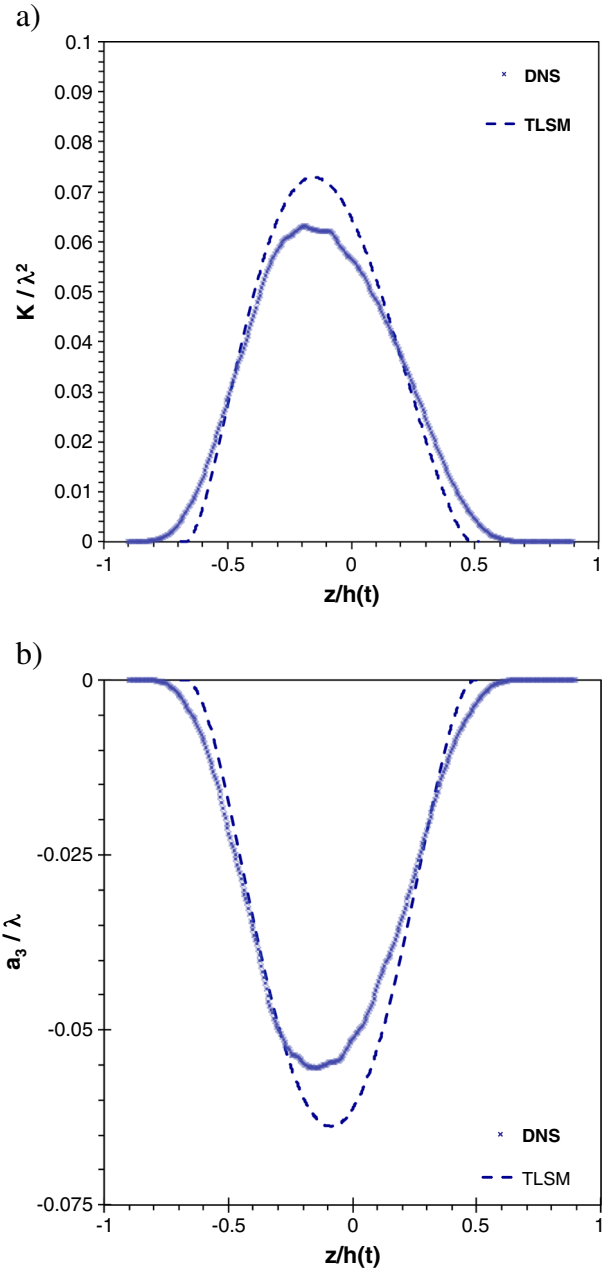

Fig. 10 Comparison of TLSM with DNS [2] for a) the turbulent kinetic energy and b) the mean mass-weighted velocity fluctuation, both for $At = 0.5$

numbers σ_a, σ_b, σ_k and σ_c were set to 1.0. However, the turbulent Schmidt numbers σ_s and σ_{2s} also affect the shear mixing layer and wall bounded flows and therefore were determined by iterating on the results. The coefficient C_4 was set to match the dimensionless growth

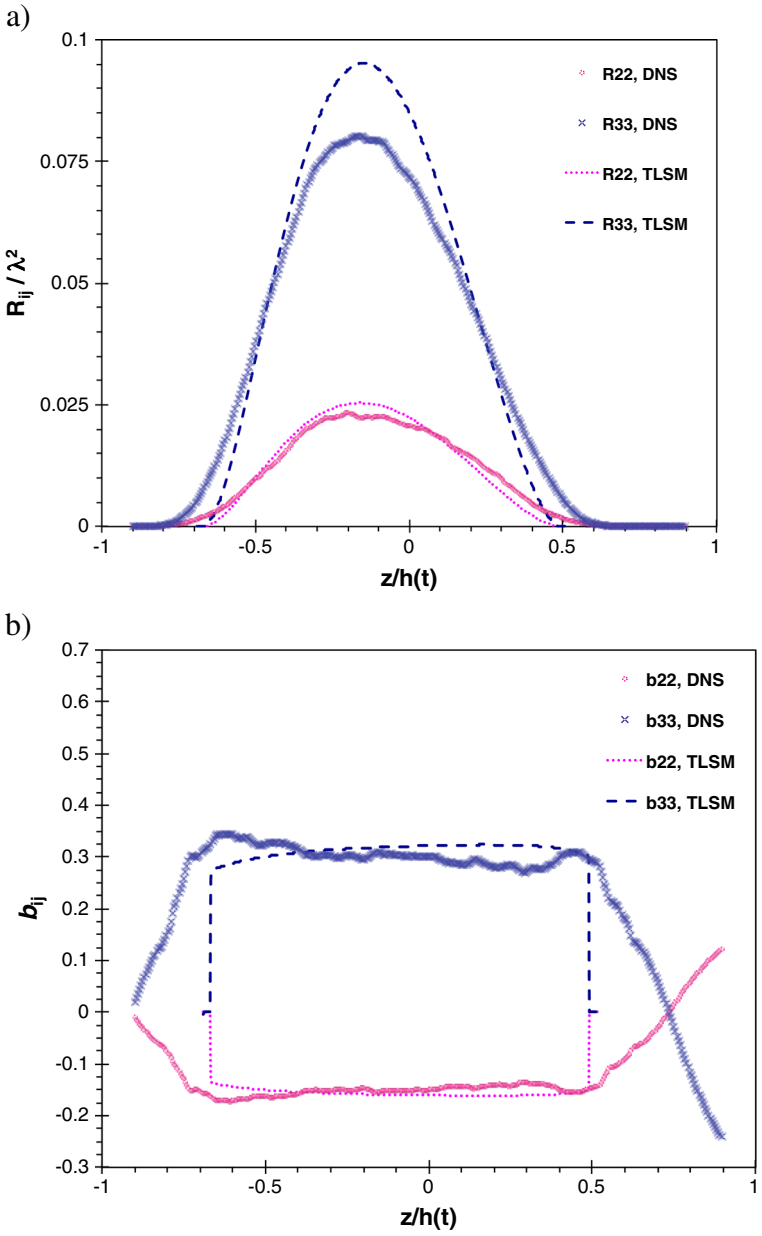

Fig. 11 Comparison of TLSM with DNS results for a) Reynolds stress and b) the anisotropic tensor, b_{ij} for $At = 0.5$

rate, α,[6] and C_{4v} was set to match HRT and α based on the assumption that $C_2 = C_{2v}$.

[6]The dimensionless growth rate parameter is given as $\alpha = \left[\left(h(t)^{1/2} - h(t_0)^{1/2}\right) / \left((Atg)^{1/2}(t - t_0)\right)\right]^2$, [8].

A direct comparison of the density profile and density-specific-volume covariance is shown in Fig. 9. Comparisons of the turbulent kinetic energy and density-turbulent-velocity

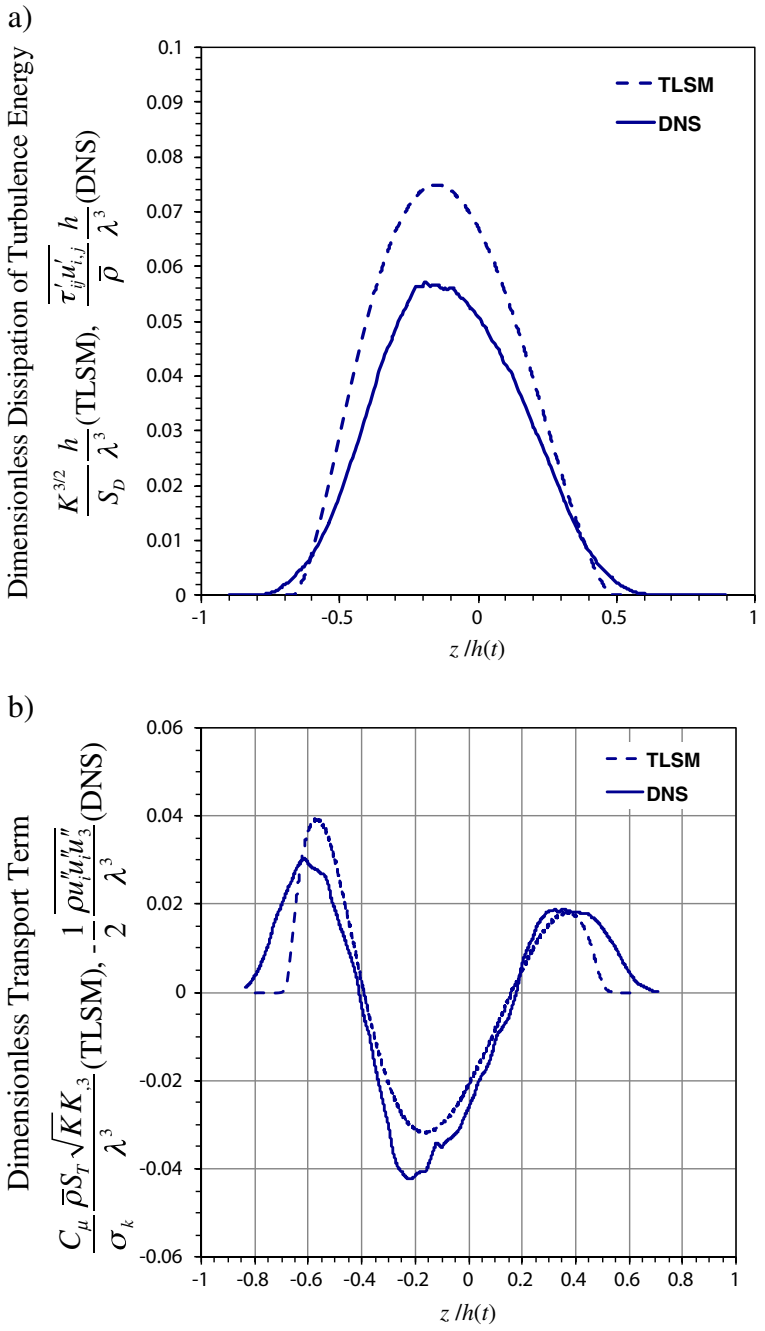

Fig. 12 A comparison of the dimensionless a) turbulence dissipation and b) transport term across the mixing region of buoyancy driven turbulence

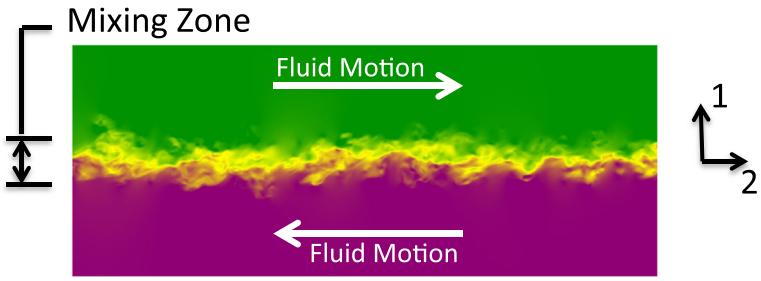

Fig. 13 DNS of the self-similar regime for a temporally developed shear layer showing the mixing zone

covariance between DNS and the model are shown in Fig. 10. A reasonable agreement is also shown for the Reynolds stress components in Fig. 11a. The anisotropic parameter $b_{\mathrm{ij}}\left(= R_{ij}/R_{kk} - \delta_{ij}/3\right)$ shows to compare reasonably with DNS (Fig. 11b). The growth rate parameter α is 0.036 for the model, compared to the DNS value of 0.0416.

In order to directly assess the pertinence of having two separate length scales, Fig. 12a compares the modeled form of the dimensionless dissipation of turbulence energy ($\varepsilon = hK^{3/2}/\lambda^3 S_D$) with the exact term ($\varepsilon = \overline{\tau'_{ij}u'_{i,j}}h/\lambda^3$) obtained from DNS and Fig. 12b compares the dimensionless modeled and the exact transport (DNS) terms in the kinetic energy equation, $\frac{C_\mu}{\sigma_k}\frac{h}{\bar{\rho}\lambda^3}\left(\bar{\rho}\, S_T \sqrt{K}\, K_{,3}\right)_{,3}$ and $-\frac{h}{2\bar{\rho}\lambda^3}\left(\overline{\rho u''_i u''_i u''_3}\right)_{,3}$, respectively. Overall, the modeled dissipation term over predicts the DNS value. The modeled transport term is close in magnitude near the edges of the mixing layer. However, the model misses the magnitude of the turbulent kinetic energy transfer from the center of the mixing layer and distributes it in a narrower region near the edges of the mixing layer. The DNS results show much longer tails near the edges than the model can capture for the variable density case. Overall, the comparison to RTI appears reasonable.

5.6 Incompressible Single Component Shear Driven Turbulence

Shear driven turbulence is generated when two fluid streams of different velocities (uniform density for this case) meet at and flow parallel to an interface, as depicted in Fig. 13. If the Reynolds number is high enough, the instability that forms along the interface transitions to turbulence creating a turbulent mixing layer between the two streams. This mixing layer continues to grow and entrain more pure fluid on either side of the interface, all the while becoming increasingly more effective at small scale mixing. For subsonic single-phase, single-component streams, the turbulent mass flux and the density-specific-volume covariance are zero. For this case, the modeled equations (16, 19-20) reduce to,

Reynolds Stress:

$$\frac{d\tilde{R}_{11}}{dt} = \underbrace{\frac{C_\mu}{\sigma_k}\left(S_T\sqrt{K}\tilde{R}_{11,1}\right)_{,1}}_{\text{Transport}} - \underbrace{C_{r3}\frac{\sqrt{K}}{S_D}\left(\tilde{R}_{11} - \frac{2}{3}K\right)}_{\text{Return to Isotropy}} - \underbrace{C_{r2}\frac{2}{3}\tilde{R}_{21}\tilde{u}_{2,1}}_{\text{Rapid Distortion}} - \underbrace{\frac{2}{3}\frac{K^{3/2}}{S_D}}_{\text{Dissipation}} \quad (37)$$

$$\frac{d\tilde{R}_{22}}{dt} = \underbrace{-2\tilde{R}_{21}\tilde{u}_{2,1}}_{\text{Production}} + \underbrace{\frac{C_\mu}{\sigma_k}\left(S_T\sqrt{K}\tilde{R}_{22,1}\right)_{,1}}_{\text{Transport}} - \underbrace{C_{r3}\frac{\sqrt{K}}{S_D}\left(\tilde{R}_{22} - \frac{2}{3}K\right)}_{\text{Return to Isotropy}} + \underbrace{C_{r2}\frac{4}{3}\tilde{R}_{21}\tilde{u}_{2,1}}_{\text{Rapid Distortion}} - \underbrace{\frac{2}{3}\frac{K^{3/2}}{S_D}}_{\text{Dissipation}} \quad (38)$$

$$\frac{d\tilde{R}_{12}}{dt} = \underbrace{-\tilde{R}_{11}\tilde{u}_{2,1}}_{\text{Production}} + \underbrace{\frac{C_\mu}{\sigma_k}\left(S_T\sqrt{K}\tilde{R}_{12,1}\right)_{,1}}_{\text{Transport}} + \underbrace{C_{r2}\tilde{R}_{11}\tilde{u}_{2,1}}_{\text{Rapid Distortion}} - \underbrace{C_{r3}\frac{\sqrt{K}}{S_D}\tilde{R}_{12}}_{\text{Return to Isotropy}} \tag{39}$$

Turbulence length scale:

$$\frac{dS_T}{dt} = \underbrace{-\frac{S_T}{K}\left(\frac{3}{2}-C_1\right)\tilde{R}_{21}\tilde{u}_{2,1} - \left(\frac{3}{2}-C_2\right)\sqrt{K}}_{\text{Net Production}} + \underbrace{\frac{C_\mu}{\sigma_s}\left(S_T\sqrt{K}S_{T,1}\right)_{,1}}_{\text{Transport}} \tag{40}$$

$$\frac{dS_D}{dt} = \underbrace{-\frac{S_D}{K}\left(\frac{3}{2}-C_{1v}\right)\tilde{R}_{21}\tilde{u}_{2,1} - \left(\frac{3}{2}-C_{2v}\right)\sqrt{K}}_{\text{Net Production}} + \underbrace{\frac{C_\mu}{\sigma_{2s}}\left(S_T\sqrt{K}S_{D,1}\right)_{,1}}_{\text{Transport}} \tag{41}$$

where index "2" refers to the streamwise direction, while "1" refers to the cross-stream direction.

The coefficients that are calibrated based on shear driven turbulence are C_1 and C_{1v}. The turbulent Schmidt numbers σ_s and σ_{2s} also affect the Rayleigh-Taylor and the von-Kármán constant in wall flows and were determined as discussed above. The turbulent Schmidt number σ_s was set to 0.1 to give a flat profile for S_T, which also affects RTI. The pressure strain terms are modeled by Rotta's [43] return to isotropy model and Naot et al.'s [44] IP model, which assumes that an energy cascade exists. As mentioned earlier, Banerjee et al. [22] studied several different pressure strain models and showed that the IP model, with $C_{r2} = 0.6$, reasonably matched contraction and expansion data when compared to modern pressure strain models, and this value also agrees with the value that comes from rapid distortion theory [19]. The coefficient associated with the slow return to isotropy, $C_{r3} = 1.8$, was given by Launder [45] and was also used by Banerjee et al. [22].

The experimental data of Bell and Mehta [46], who studied a spatially growing layer, and a new DNS run of a temporally growing layer, similar to the simulation of Riley, Metcalfe and Orszag [47], are mainly used for this calibration. For the spatially evolving case, the derivatives of the mean quantities in the spanwise direction are zero, while the temporal case assumes periodic boundaries in both the spanwise and streamwise directions, resulting in derivatives of the mean quantities being zero in these directions. The new DNS run was performed in order to provide data for the two-length scale model, which could not be extracted from previous experiments or simulations. The set-up for the simulation is based on Riley et al. [47], although the present domain is much larger and the initial energy spectrum is different. The simulation is initialized with a hyperbolic tangent velocity profile to represent the shear layer and an initial perturbation consisting of isotropic turbulence that is tapered such that the intensity decays away from the interface in the base velocity profile. Following Riley et al. [47], the root mean square (RMS) intensity is tapered by a Gaussian function selected to match laboratory data as $\exp[-x_1/(0.653\ h_0)]^2$, where h_0 is the initial thickness between the x_1 positions at which the mean velocity profile corresponds to 10 % and 90 % of the difference between the free mean velocities [19]. The isotropic turbulence is specified such that its energy spectrum behaves as $(k/k_0)^4\exp[-2(k/k_0)^2]$, where the peak wavenumber k_0 is chosen to be $3.92/h_0$. The corresponding peak wavelength is one-fourth the wavelength of the least stable mode for an inviscid hyperbolic tangent mixing layer, so the energy distribution includes significant energy in the scales of motion finer than those with the fastest linear growth rate. The streamwise domain length (described below) was chosen to accommodate 64 least stable modes, and thus the domain can accommodate 256

peak wavelengths (based on k_0). The RMS intensity at the peak of the profile is selected to be nominally $0.1(U_{fast} - U_{slow})$ in each component, but the intensity slightly deviates from isotropy due to requiring that the tapered disturbance field be divergence-free. The viscosity was chosen such that the initial Reynolds number would be 80 based on the initial momentum thickness and characteristic velocity difference $U_s = U_{fast} - U_{slow}$. For the initial hyperbolic tangent velocity profile, the momentum thickness is 0.228 h.

The simulation was performed with the CFDNS code [48] that was also used for Rayleigh-Taylor instability simulations [49–51]. Fourier spectral representations were used in the periodic (spanwise and streamwise) directions, while 6$^{\text{th}}$ order compact finite differences were used in the inhomogeneous (transverse) direction. Slip walls are used to represent the upper and lower boundaries of the shearing fluid layers. A third order variable time step Adams-Bashforth-Moulton scheme [52], coupled with a pressure projection method, was used for time advancement. The domain size is $410.3h_0$, $78.5h_0$, and $102.6h_0$ in the streamwise, transverse, and spanwise directions, respectively, and the corresponding numbers of grid points are 3072, 720, and 768. The DNS reaches a self-similar growth regime. The mean and RMS statistics are consistent with other shear-driven mixing layer DNS studies, such as Rogers and Moser [53] and Pantano and Sarkar [54]. In separate simulations [55], the CFDNS code was demonstrated to very closely reproduce the results of Rogers and Moser [56]. For the two data sets used for calibration, the momentum thickness Reynolds numbers range up to 6000 for the Bell & Mehta experiment [46] (according to [53]) and up to 1350 in the present DNS. Based on thickness h, the Reynolds number Re_h for the present DNS ranges up to 6250.

In this study, the model was set up as a temporally growing layer. For shear induced turbulence the turbulent kinetic energy was initialized as $K_0 = \zeta U_s^2$ where ζ is the turbulence intensity ($<<1$ %). The turbulent kinetic energy was isotropically distributed across the diagonal components of the Reynolds stress tensor, while the off-diagonal components were initialized to zero. The turbulent length scale was initialized to a very small value and a_i and b were initialized as zero. The model was ran well into a self-similar regime where $\text{d}K/\text{dt} \sim 0$ at the centerline of the flow.

The Reynolds stress components are non-dimensionalized by the square of the velocity difference (U_s^2) and compared in Fig. 14a. Overall, the second moment closure is in reasonable agreement with the two datasets. The mean velocity profile, shown in Fig. 14b, compares well with the error function theory (described in [19, 48]), the experimental data and DNS in the self-similar regime. The self-similar spreading rate (β) of a temporal shear driven mixing layer is given by $\beta \approx d\delta \big/ (U_s dt)$ where δ is the mixing layer width [19]. A reasonable agreement between a) the magnitudes and profile of the Reynolds stress components, b) the growth rate of the shear layer and c) homogeneous shear was found by setting C_{1v} to 1.3 and C_1 to 1.6. The growth rate parameter from the model is $\beta = 0.056$, compared to 0.064 for the DNS and 0.076 [46] for the experiment. When calculated based on momentum thickness, the growth rate β_m for the model is 0.012, which is in good agreement with the value of 0.013 calculated from the DNS (and 0.014 obtained in DNS by Rogers and Moser [53]). The finalized coefficients are shown in Table 1.

An assessment of the two-length scale model is shown in Fig. 15, where Fig. 15a compares the modeled dimensionless dissipation of turbulence energy, $\varepsilon = K^{3/2}h/(S_D U_s^3)$, with the exact dissipation term $\varepsilon = \overline{\tau'_{ij} u'_{i,j}} h/\bar{\rho} U_s^3$ obtained from DNS, and Fig. 15b compares the dimensionless modeled and exact transport (DNS) terms in the kinetic energy equation, $\frac{C_\mu}{\sigma_k} \frac{h}{U_s^3} \left(S_T \sqrt{K} K_{,1} \right)_{,1}$ and $-\frac{h}{2U_s^3} \left(\overline{u'_i u'_i u'_1} \right)_{,1}$, respectively. Overall, a reasonable match is obtained for both quantities. Similar to RTI, the uniform density shear case shows

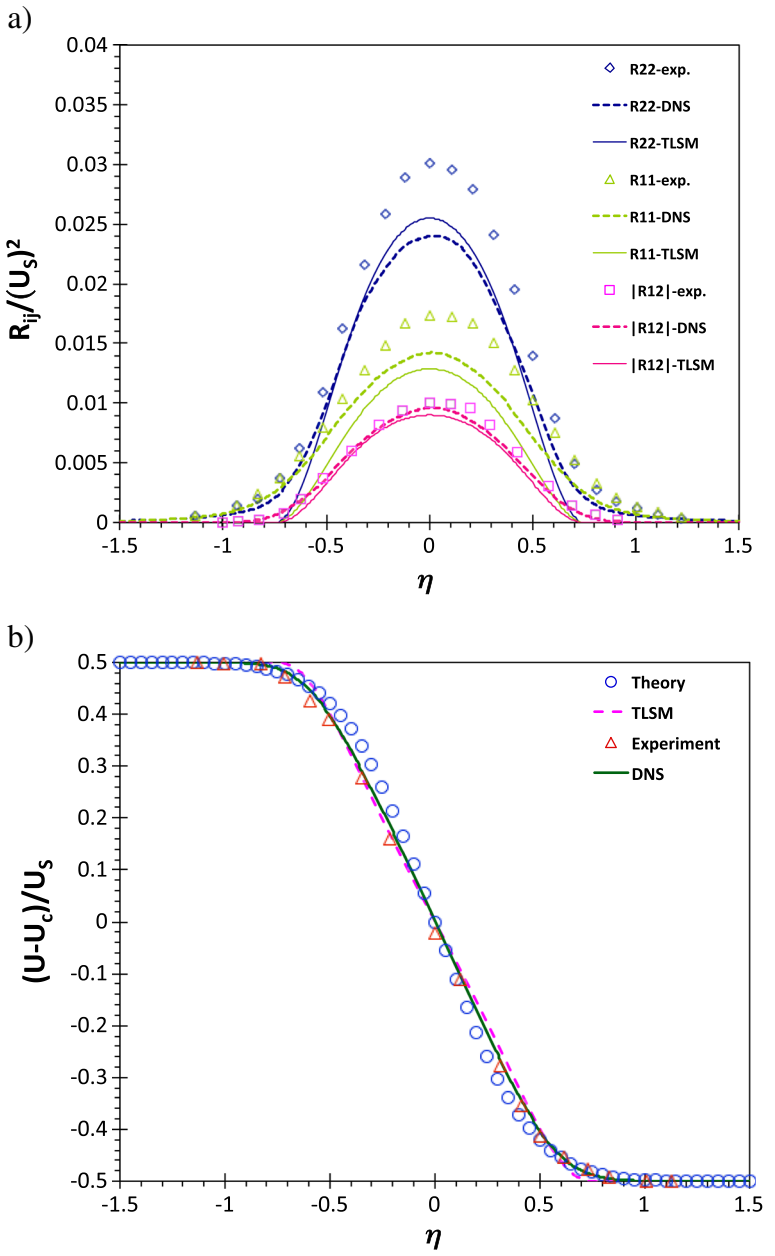

Fig. 14 Comparison of the TLSM with DNS results and experimental data (Bell and Mehta [36]) for a) Reynolds stress components, and b) dimensionless velocity profile. $U_s = U_{fast} - U_{slow}$, $\eta = (x_1\text{-}x_{cl})/\delta$, where x_{cl} is the x_1 value at the centerline of the mixing layer

that the model is missing the transfer of turbulence kinetic energy from the interior of the layer to the edges of the shear layer. When comparing the trends of the transport term (Fig. 15b) with the RT transport term (Fig. 12b), one notices a symmetric form associated

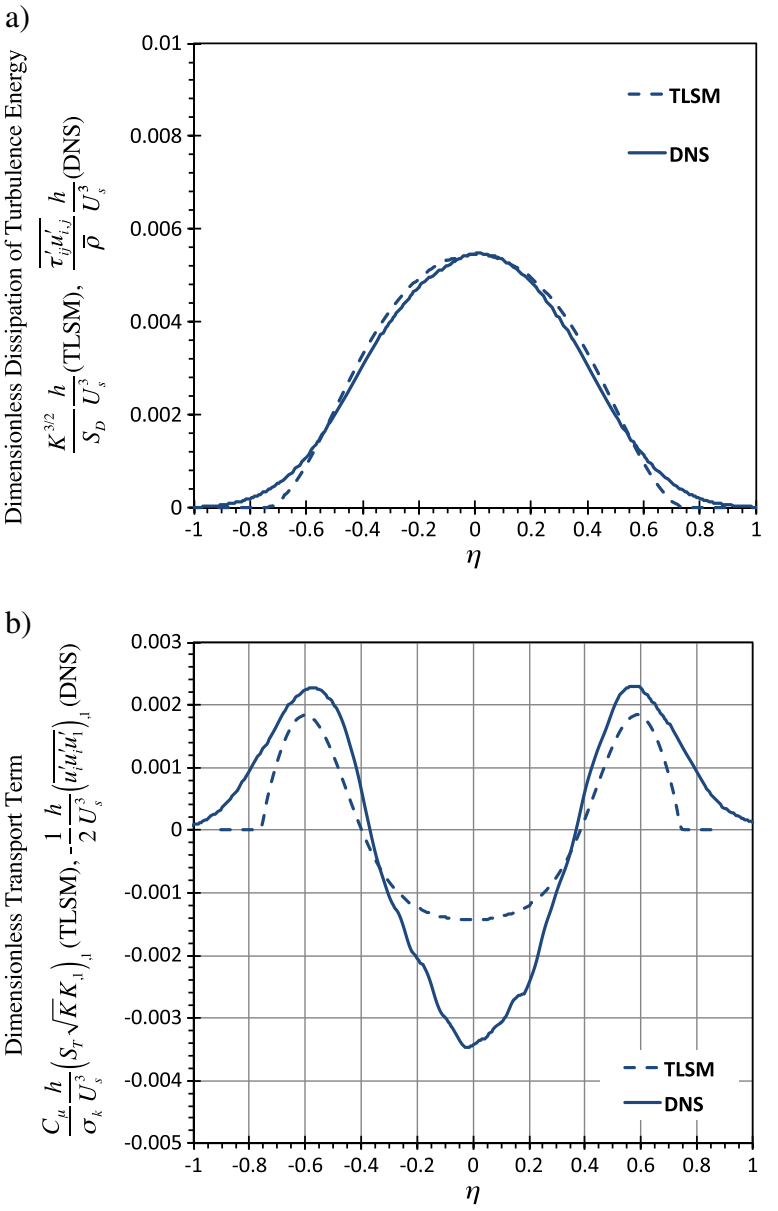

Fig. 15 A comparison of dimensionless a) turbulence dissipation and b) transport term across the mixing region of a shear layer

with the uniform density shear transport and an asymmetric form associated with the variable density RT transport. This asymmetry is primarily driven by the coupling between density-specific-volume covariance (b) and turbulence mass flux ($\bar{\rho}a_1$) to skew S_T and K, and one might expect these parameters to influence the transport terms for the variable density case without affecting the uniform density case.

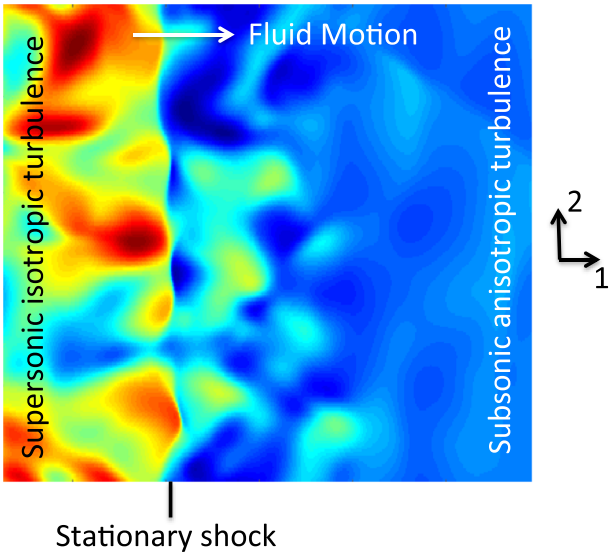

Fig. 16 Single fluid shocked isotropic turbulence (produced by DNS used in studies [60, 61]). The fluid is supersonic with $M_{shock} = 1.2$ and $M_{turb} = 0.24$ prior to the shock and transitions to subsonic after the shock

5.7 Single-phase, Single Component Shocked Isotropic Turbulence

The standard problem of a shock passing over single fluid homogeneous isotropic turbulence (shown in Fig. 16) is an important test case for any model of variable density turbulent flows. In particular, the ability to demonstrate that the model is physically justified for this flow is a precursor for the more complicated Richtmyer-Meshkov (RM) flows. For this type of flow, the mean fields are 1D, so that the modeled equations (16-20) are simplified to

Reynolds Stress:

$$\frac{\partial\left(\bar{\rho}\tilde{R}_{11}\right)}{\partial t}+\left(\bar{\rho}\tilde{u}_1\tilde{R}_{11}\right)_{,1}=\overbrace{2a_1\bar{P}_{,1}-2\bar{\rho}\tilde{R}_{11}\tilde{u}_{1,1}}^{\text{Production}}+\overbrace{\frac{C_\mu}{\sigma_k}\left(\bar{\rho}S_T\sqrt{K}\tilde{R}_{11,1}\right)_{,1}}^{\text{Transport}}-\overbrace{C_{r3}\bar{\rho}\frac{\sqrt{K}}{S_D}\left(\tilde{R}_{11}-\frac{2}{3}K\right)}^{\text{Return to Isotropy}}$$
$$+\underbrace{\frac{4}{3}\left(C_{r2}\bar{\rho}\tilde{R}_{11}\tilde{u}_{1,1}-C_{r1}a_1\bar{P}_{,1}\right)}_{\text{Rapid Distortion}}-\underbrace{\bar{\rho}\frac{2}{3}\frac{K^{3/2}}{S_D}}_{\text{Dissipation}} \tag{42}$$

$$\frac{\partial\left(\bar{\rho}\tilde{R}_{22}\right)}{\partial t}+\left(\bar{\rho}\tilde{u}_1\tilde{R}_{22}\right)_{,1}=\overbrace{\frac{C_\mu}{\sigma_k}\left(\bar{\rho}S_T\sqrt{K}\tilde{R}_{22,1}\right)_{,1}}^{\text{Transport}}-\overbrace{C_{r3}\bar{\rho}\frac{\sqrt{K}}{S_D}\left(\tilde{R}_{22}-\frac{2}{3}K\right)}^{\text{Return to Isotropy}}$$
$$-\underbrace{\frac{2}{3}\left(C_{r2}\bar{\rho}\tilde{R}_{11}\tilde{u}_{1,1}-C_{r1}a_1\bar{P}_{,1}\right)}_{\text{Rapid Distortion}}-\underbrace{\bar{\rho}\frac{2}{3}\frac{K^{3/2}}{S_D}}_{\text{Dissipation}} \tag{43}$$

Turbulence mass flux:

$$\frac{\partial\left(\bar{\rho}a_1\right)}{\partial t}+\left(\bar{\rho}\tilde{u}_1a_1\right)_{,1}=\underbrace{\left(1-C_{ap}\right)b\bar{P}_{,1}-\tilde{R}_{11}\bar{\rho}_{,1}-\left(1-C_{au}\right)\bar{\rho}a_1\bar{u}_{1,1}}_{\text{Net Production}}+\underbrace{\bar{\rho}\left(a_1a_1\right)_{,1}}_{\text{Redistribution}}$$
$$+\underbrace{\bar{\rho}\frac{C_\mu}{\sigma_a}\left(S_T\sqrt{K}a_{1,1}\right)_{,1}}_{\text{Transport}}-\underbrace{C_{a1}\bar{\rho}\frac{\sqrt{K}}{S_D}a_1}_{\text{Destruction}} \tag{44}$$

Density-specific-volume covariance:

$$\frac{\partial\left(\bar{\rho}b\right)}{\partial t}+\left(\bar{\rho}b\tilde{u}_1\right)_{,1}=-\underbrace{2\left(b+1\right)a_1\bar{\rho}_{,1}}_{\text{Production}}+\underbrace{2\bar{\rho}a_1b_{,1}}_{\text{Redistribution}}+\underbrace{\bar{\rho}^2\frac{C_\mu}{\sigma_b}\left(\frac{1}{\bar{\rho}}S_T\sqrt{K}b_{,1}\right)_{,1}}_{\text{Transport}}-\underbrace{C_{b1}\bar{\rho}\frac{\sqrt{K}}{S_D}b}_{\text{Dissipation}} \tag{45}$$

Turbulence length scale:

$$\frac{\partial\left(\bar{\rho}S_T\right)}{\partial t}+\left(\bar{\rho}\tilde{u}_1S_T\right)_{,1}=\underbrace{-\frac{S_T}{K}\left(\frac{3}{2}-C_1\right)\bar{\rho}\tilde{R}_{11}\tilde{u}_{1,1}+\frac{S_T}{K}\left(\frac{3}{2}-C_4\right)a_1\bar{P}_{,1}-\left(\frac{3}{2}-C_2\right)\bar{\rho}\sqrt{K}}_{\text{Net Production}}$$
$$+\underbrace{\frac{C_\mu}{\sigma_s}\left(\bar{\rho}S_T\sqrt{K}S_{T,1}\right)_{,1}}_{\text{Transport}} \tag{46}$$

$$\frac{\partial\left(\bar{\rho}S_D\right)}{\partial t}+\left(\bar{\rho}\tilde{u}_1S_D\right)_{,1}=\underbrace{-\frac{S_D}{K}\left(\frac{3}{2}-C_{1v}\right)\bar{\rho}\tilde{R}_{11}\tilde{u}_{1,1}+\frac{S_D}{K}\left(\frac{3}{2}-C_{4v}\right)a_1\bar{P}_{,1}-\left(\frac{3}{2}-C_{2v}\right)\bar{\rho}\sqrt{K}}_{\text{Net Production}}$$
$$+\underbrace{\frac{C_\mu}{\sigma_{2s}}\left(\bar{\rho}S_T\sqrt{K}S_{D,1}\right)_{,1}}_{\text{Transport}} \tag{47}$$

where index "1" denotes the streamwise direction, while "2" one of the periodic directions in the plane of the shock (Fig. 16).

While this flow is an important test case, the available data are not as well understood. For example, the experiments of Agui, et al. [57] and Barre et al. [58] versus the DNS of Lee et al. [59] show large discrepancies in the turbulence enhancement effects of the shock. However, recent results have clarified the turbulence jump through the shock in the limit of a large-scale separation between turbulence and shock width, for low incoming turbulent Mach number [60, 61]. Thus, in this limit, the results become close to the Linear Interaction Approximation (LIA) predictions [62, 63]. Since in many practical applications the shock width is much smaller than the turbulence length scales, while the turbulent Mach number of the incoming turbulence is small, we choose to use LIA as a comparing factor.

The principal result is shown in Fig. 17 where the jump in R_{11} and R_{22} is given for the model and the LIA for various Mach numbers. The results shown in Fig. 17 for the TLSM were produced by setting C_{au} to 0.4; setting $C_{\text{au}} = 0.0$ caused a decrease in R_{11} while a value of 1.0 caused the jump in R_{11} to be greater than 3.

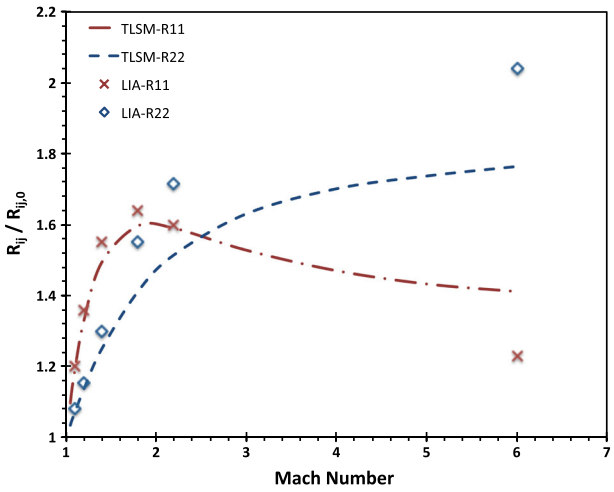

Fig. 17 Comparison of the TLSM to LIA theory showing the "roll over" effect of R_{11} near Mach 2. The transition of R_{22} (orthogonal to the direction of the shock) also agrees with LIA showing that more turbulent energy is transferred to the transverse components (R_{22}) relative to the pre-shock values ($R_{22,0}$)

The reason for the significance of C_{au} is because of the balance of terms across the shock. The model (as does LIA) has production dominating over dissipation and transport when integrated over the shock width. The production/dissipation ratio is roughly 1.0e6 for the cases explored in the model and is essentially infinite in the LIA. As such, the length scale does not play a role in the turbulent enhancement. The net production in the R_{11} equation has a Mach number effect; at low M the $a_1 \mathrm{d}P/\mathrm{d}x_1$ term has less of an effect than at high M; for example at $M = 1.2$, $a_1 \mathrm{d}P/\mathrm{d}x_1$ is 40 % and opposite sign of the $\rho R_{11} \mathrm{d}U/\mathrm{d}x_1$ production term, at higher M (greater than 1.8) the $a_1 \mathrm{d}P/\mathrm{d}x_1$ term is still opposite sign but is ~ 90 % of the $\rho R_{11} \mathrm{d}U/\mathrm{d}x_1$ term. This shows the importance of getting the turbulent mass flux correct at higher M and is the reason for setting C_{au}.

Initialization and resolution play an important role in modeling shocked flows; however initialization did not affect the results significantly for the present case. The initial turbulent kinetic energy was varied between 0.1 and 1.0e5 $\mathrm{cm}^2/\mathrm{s}^2$ (in all cases the turbulent Mach number was kept below 0.01), and the initial length scales were varied from 0.1 to 40 cm, all of which showed no effect on the turbulent enhancement. The values of a_1 and b were initialized to zero in front of the shock.

Grid resolution plays a key role in shocked flows. This holds true regardless of whether the simulation being explored is DNS, Large Eddy Simulation (LES) or Reynolds (or Favre) Averaged Navier-Stokes (RANS). The work of Singh et al. [64] showed how a simple algebraic form for the Reynolds stress couldn't maintain convergence on resolution. The present model (R_{ij} transport equations) converges upon mesh refinement for the turbulent enhancement relative to the pre-shock value (i.e. R_{11} / $R_{11,0}$). The enhancement is given for $M =$ 1.4, 2.2 and 5.0 as a function of resolution and shown in Fig. 18, where the abscissa, $\vartheta = (S_{\mathrm{T}} K^{1/2})/(\Delta x V_{\mathrm{s}})$ is dimensionless with finer resolutions to the right. A transition is noticed between $\vartheta = 0.1 - 3$, where values larger than $\vartheta = 3$ show a convergence on the shock width. At the lower resolution, $\vartheta <$0.1, the shock width is determined by numerical diffusion (in this case around 4 cells thick). Upon refining the resolution, the shock width is

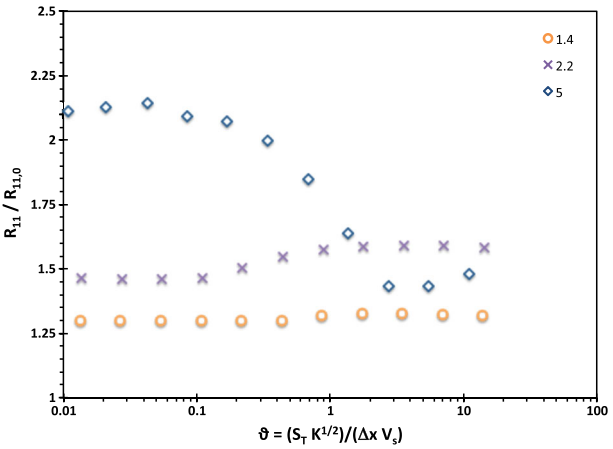

Fig. 18 Resolving the turbulence energy across the shock requires very fine resolution. For M = 1.4 – 5 (shown in legend), a transition in the post shock R_{11} is seen between $\vartheta = 0.1$ and 3. S_T is the pre-shocked turbulent length scale, K is the pre-shocked turbulent kinetic energy, V_s is the shock speed and Δx is the zone size

essentially set based on a turbulent viscosity and no longer changes with cell size (S_T and $S_D >> \Delta x$). The turbulence enhancement, relative to the pre-shock values, can be very different amongst the diagonal components in the Reynolds stress at high M, and if under-resolved, the roll over for R_{11} / $R_{11,0}$ at $M \sim 2$ (shown in Fig. 17) may not be present.

6 Model Coefficients

Based on the above fundamental studies, the model coefficients were found from DNS, experimental data and theory, for shear, buoyancy and shock driven turbulence. A list of coefficients is shown in Table 1. Overall, it was found that C_4 is the major contributor to the RT mixing layer growth while C_{4v} is a major contributor to the magnitudes of the turbulence statistics in both RT and HRT. Likewise, C_1 is a major contributor to the shear driven mixing layer growth and C_{1v} is a major contributor to magnitude of the turbulence statistics. For shocked isotropic turbulence, the rapid decay model for the turbulence mass flux showed a reasonable match to LIA prediction with $C_{au} = 0.4$ and a closer match to experimental data for isotropic turbulence decay was made with $C_2 = C_{2v} = 1.77$ (or $C_{\varepsilon 2}$ for the k-ε model [19]).

If a reasonable match cannot be obtained with a common set of models and coefficients, then confidence dwindles when trying to simulate turbulence in more complicated flow regimes such as shock driven turbulence where density, pressure and velocity gradients may simultaneously exist. Modeling transport and dissipation terms obtained by Reynolds or Favre averaging requires making approximations and assumptions, and there is a great deal of latitude in the forms used for modeling these terms and the methodology for calibrating the coefficients. However, we have demonstrated that using DNS to understand the physics and carefully calibrate coefficients for a fundamental set of turbulence flows can provide reasonable agreement between RANS type models, DNS and measurable physics.

7 Application to Flows Not used for Calibration

To assess the ability of the TLSM to predict flows beyond the range of flows that were used to calibrate it, we seek to apply it to cases that introduce additional complexity to the flows previously considered, yet were not involved in the calibration. The model can be applied to two interesting flows that contain similar physics, namely 1) variable density shear driven turbulence and 2) shock driven variable density mixing, also referred to as Richtmyer-Meshkov instability driven turbulence.

7.1 Variable Density Shear Driven Turbulence

In order to assess the capability of the newly calibrated RANS model to capture the physics of a mixing layer in which non-buoyant variable density effects are introduced, a new data set is required. To fulfill this, a DNS simulation of the temporally developing variable density mixing layer with a zero body force was performed with CFDNS using the same approach and similar parameters to the single-fluid mixing layer simulation (described in Section 5.6). The flow/setup is shown in Fig. 13, except the two streams contain different density fluids. The hyperbolic tangent mean velocity profile is retained with the same thickness, again resulting in an initial momentum thickness of 80. The density difference between the streams of fluids is introduced by prescribing a mean density variation with a hyperbolic tangent profile aligned with and of the same width at the velocity profile. The densities are chosen to produce $At = 0.75$, which corresponds to a density ratio of 7, similar to a mixing layer between nitrogen and helium. For the DNS, the kinematic viscosities of each fluid and mass diffusivity are chosen to have constant values, such that the Schmidt number is uniform with a value of unity everywhere within the fluid.

Compared to the single-fluid case in Section 5.6, the domain length and width are each reduced to half. This results in streamwise and spanwise dimensions of $205.5h_0$ and $51.4h_0$, with 2048 and 512 grid points resolving each direction. Relative to the single-fluid mixing layer DNS, however, the cross-stream direction is enlarged to $104.9h_0$ and resolved with 1280 grid points, to ensure that the growth of the mixing layer toward both the light and heavy fluid sides is unaffected by the presence of the slip walls bounding the sides of the domain. Relative to the single-fluid mixing layer, the resolution (in terms of grid points per length) is increased proportionally in each direction due to the more stringent resolution requirements when significant density gradients are also present.

As with the single-fluid mixing layer, initial velocity fluctuations are introduced to trigger the instability leading to turbulence. However, no additional perturbations are added to the density field. The initial profile of the velocity disturbance is the same as that used for the single fluid case, and the spectrum of this disturbance has the same form, amplitude, and peak wavenumber.

The simulation proceeds until the mixing layer reaches a self-similar growth regime and a Reynolds number $\mathrm{Re_h}$ of 7440, which corresponds to a momentum thickness Reynolds number of 910. Though the former Reynolds number slightly exceeds that of the single-fluid mixing layer DNS, the momentum thickness Reynolds number is somewhat lower because the mean velocity profile center shifts to the light fluid side and, by definition, momentum thickness is weighted by the fluid density.

The corresponding RANS simulations follow a similar temporal set-up. The centerline of the mixing layer was initially aligned between the RANS simulation and the DNS to set the zero point of the mixing layer. The density difference between streams was introduced by specifying two ideal gases characterized the same γ values but different $\mathrm{C_v}$ values. These

mean fluid properties are chosen to approximate those of nitrogen, but the C_v values are changed from this mean to obtain the desired Atwood number of 0.75. The fluid is initially in equilibrium with 1 atm constant pressure and a high constant temperature, which is chosen such that the nominal Mach number is less than 0.1; this ensures good adherence to the incompressible flow simulated by the DNS. As with the uniform density mixing layer, there is initially a step discontinuity in velocity at the interface. The densities of the streams are prescribed by also introducing a step discontinuity in density at this interface by specifying different fluids on each side. The turbulent length scale, a_i, and b were initialized in accord with the uniform density flow, and the initial turbulent kinetic energy was prescribed as described for that case, with K_0 chosen to be approximately 1 % of U_s^2.

Statistics were obtained after the flow reached self-similarity. Self-similarity was verified by observing that the thickness growth rates were linear with respect to time, verifying that the peak values of flow statistics (e.g., R_{ij} and b) were constant with respect to time, and checking that statistical profiles (e.g., U and ρ) did not vary with time when x was scaled by thickness, while ensuring that the profiles remained at the free-stream values at the boundaries of the transverse domain. Additionally, a resolution study was performed, which indicated that the self-similar quantities agreed within several percent when the grid spacing was refined by a factor of four. The grids remained fixed for both the uniform density and variable density mixing layers as AMR was not used for these cases.

The β growth rate (described in Section 5.6) is 0.05 in DNS and 0.053 with the model; the $\beta_m = (d\delta_m/dt)/U_s$ momentum thickness growth rate is 0.0054 in the DNS and 0.0059 in the model. Thus, the model correctly captures the trends observed in the variable density mixing layer DNS. Relative to the single-fluid case, the β_m growth rate is reduced much more significantly because this measurement is sensitive to the mean velocity profile center shift, as noted above.

A comparison of the dimensionless velocity is shown in Fig. 19. The model appears to capture the shift in the mean velocity from the initial point. A comparison of the density and density-specific-volume covariance (b) is shown in Figs. 20a and 20b, respectively,

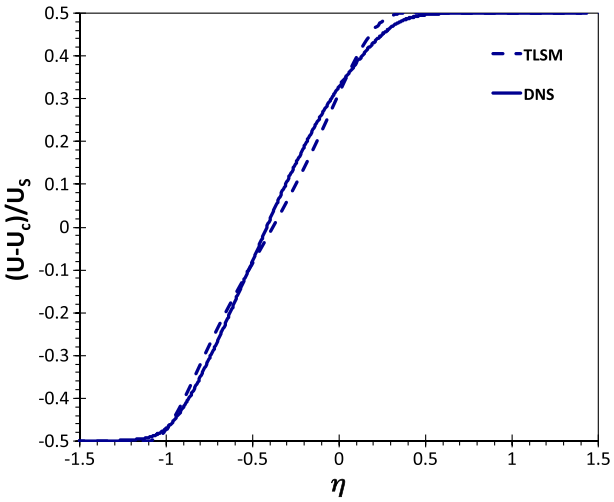

Fig. 19 Comparison of the dimensionless velocity across the variable density shear layer, $At = 0.75$ (solid lines – DNS, dashed lines– TLSM). For the temporal developing layer, $U_c = 0$, the shift in the velocity profile towards the heavy fluid is consistent (initially at $\eta = 0$, $U = 0$)

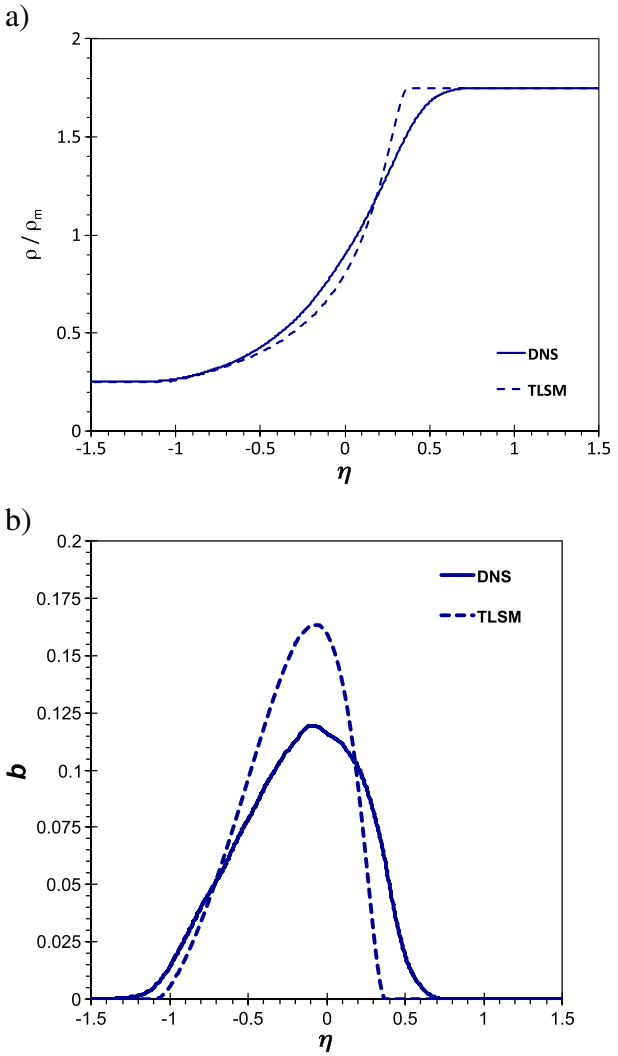

Fig. 20 Comparison of a) the dimensionless density profile and b) the density-specific-volume covariance across the variable density shear layer, $At = 0.75$ (solid lines – DNS, dashed lines – TLSM)

where $\rho_m = (\rho_{\text{high}} + \rho_{\text{low}})/2$. The comparison is also reasonable, showing the sharp rise in density on the heavy side fluid and the peak of b just slightly shifted towards the lighter fluid side. Additional comparisons of the Reynolds stress and the mean mass-weighted velocity fluctuation are shown in Figs. 21a and 21b, respectively. Though the magnitude of a_1 is under predicted (by approximately 40 %), the shape of the curve is correct. The magnitude of a_2 matches the DNS more closely, with a slight misalignment of the peak. Despite the differences in a_i and b, the results show that the predictions of the two-length scale RANS model, as calibrated by the preceding flows, reasonably captures the behavior of this new flow. The dimensionless dissipation and transport terms are compared in Fig. 22. Overall, these quantities also appear to be in reasonable agreement.

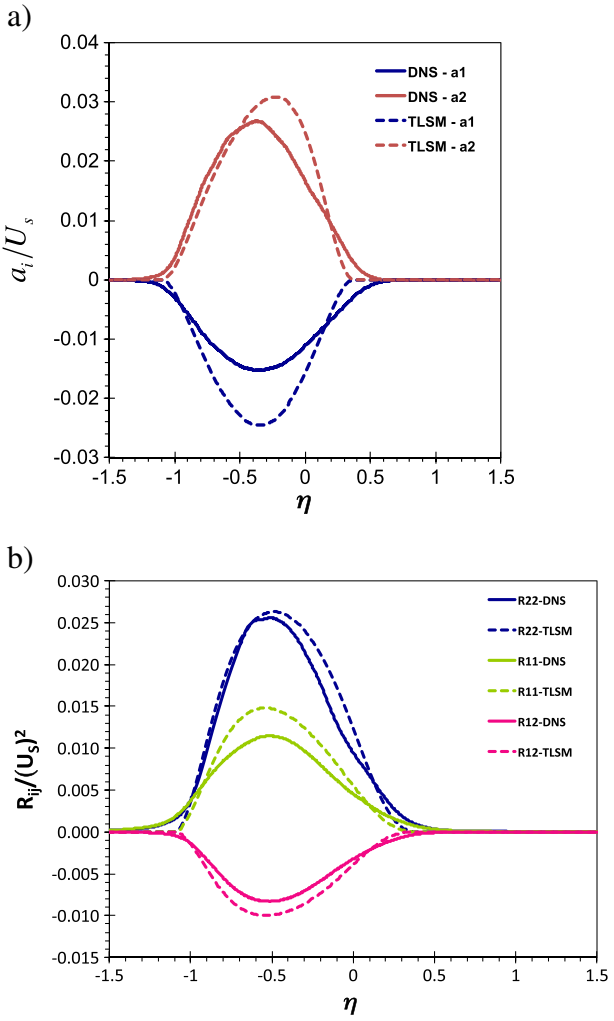

Fig. 21 Comparison of a) the dimensionless mean mass-weighted velocity fluctuation and b) the Favre averaged Reynolds stress across the variable density shear layer, $At = 0.75$ (solid lines – DNS, dashed lines – TLSM)

7.2 Shock Driven Variable Density Mixing

Richtmyer-Meshkov instability (RMI) describes the features that develop after a shock passes over a perturbed interface between two different density fluids [65, 66]. Depending on the strength of the shock, the viscosity of the fluids, and the amplitude and wavelength of the initial perturbation, the instability can rapidly (or slowly) transition to turbulence, or possibly never reach a fully developed turbulent state. However, a re-shocked interface (which occurs when the shock reflects off the end of the shock tube and travels back towards the mixing zone, depicted in Fig. 23) can also generate turbulence. Unlike the previous flows considered, RMI induced turbulence does not reach a self-similar form and,

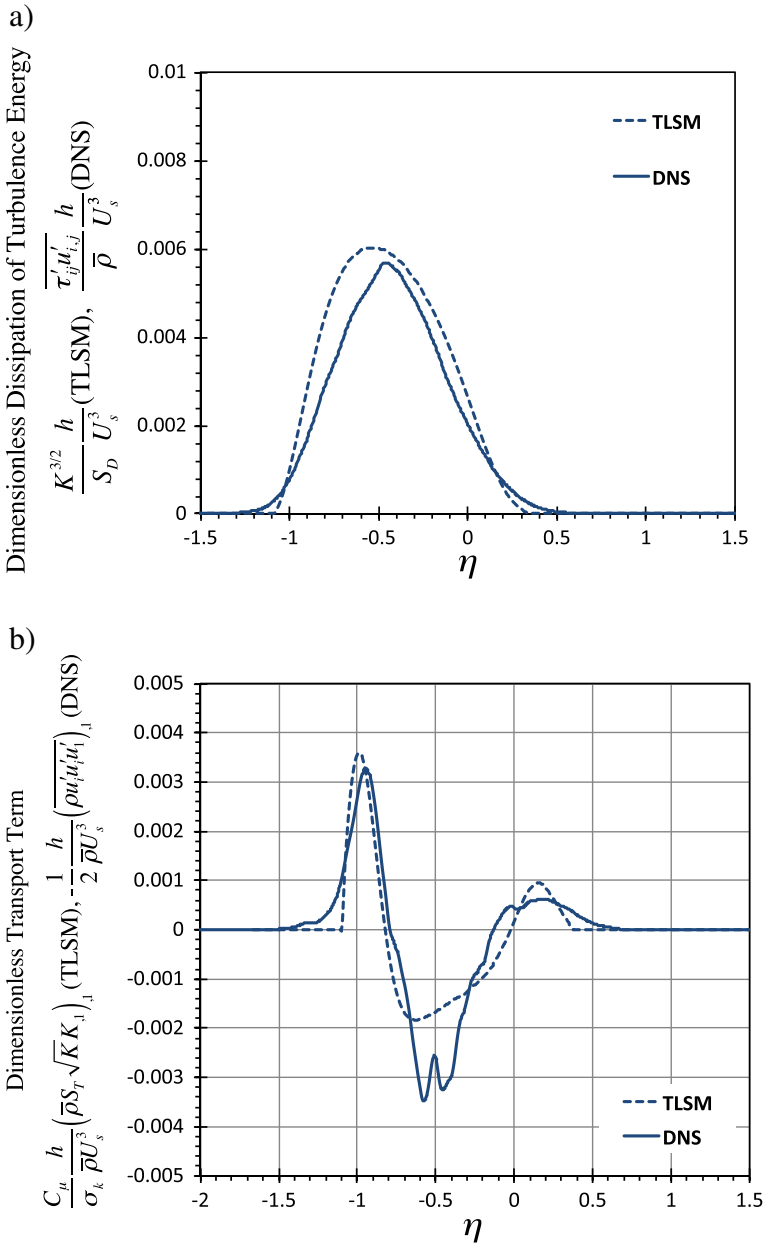

Fig. 22 Comparison of a) the turbulence dissipation and b) the transport terms across the variable density shear layer, $At = 0.75$ (solid lines – DNS, dashed lines – TLSM)

as a consequence, may challenge the turbulence models that were developed using this assumption.

One of the problems with shock tube data of RMI generated turbulence is the shock-wave/boundary-layer interaction, which can become important in modest sized shock tubes.

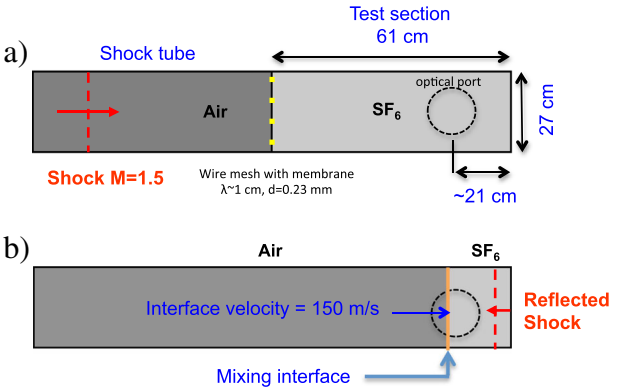

Fig. 23 Schematic of the horizontal shock tube, a) at $t = 0$, and b) just before re-shock

Vetter and Sturtevant [67] proposed to minimize this effect by taking data in a larger (27 cm square) test section. Their experimental apparatus consisted of a horizontal shock tube with the ability to use various length test sections (0.61 to 1.22 m). A nitro-cellulose membrane (0.5 μm thick) was used to separate the high- and low-pressure fluids, creating the "interface". They experimented with the placement and size of the wire mesh, which was partially used to set the perturbations.

Although the shock tube problem is inherently 3D, due to the boundary layer development along the walls of the shock tube and the initialization of instabilities due to the wire mesh, we attempt a simple 1D comparison. The reason for this simplification is that the RAGE hydrocode was not developed for wall flows (e.g. capturing the velocity gradient of the fluid within the turbulent boundary layer). For the 1D case, the governing equations (13-20) can be simplified. The initial conditions used were $K_0 = \zeta \Delta U^2$, where ΔU is the jump velocity of the interface and ζ is the turbulence intensity ($<<1$ %), and $S_{D0} = S_{T0} =$ 1.0 cm, based on the wavelength of the mesh, $a_1(t = 0)$ was set to zero and b_0 was set to the immiscible value near the interface.

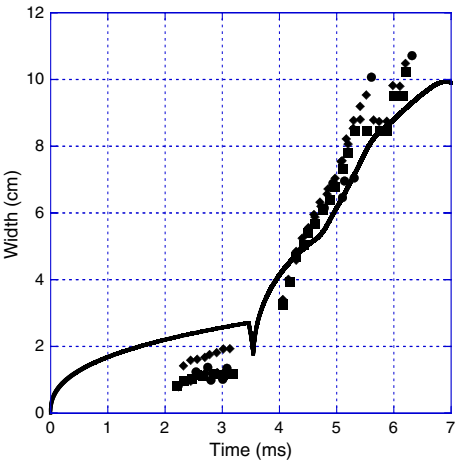

Fig. 24 Comparison of the of the mixing layer width for shock driven turbulence, both before and after re-shock ($\sim$ 3.5 ms), $M = 1.5, At = 0.75$ (solid line – TLSM, symbols – experimental data). The different symbols represent the various initial conditions associated with wire-mesh-membrane arrangement between air and SF_6, see [67] for more details

Vetter and Sturtevant [67] used schlieren images to capture the growth of the mixing zone. However, the method used to measure the mix width was not discussed; therefore the uncertainty is unknown and as a result comparisons of the growth rate of the layer are typically made [68]. In the simulation, we determined the width of the mixing layer based on ~ 5 % concentration level. This was plotted and compared with the experimental data, shown in Fig. 24. The model compares reasonably well with the experimental data after re-shock, however it over predicts the width of the mixing layer after first shock. The over prediction after first shock is not unusual; [68] and [69] show similar trends using large eddy simulations. Based on the schlieren images shown in [67], the mix width after re-shock appears to have less uncertainty than the mix width values prior to re-shock.

8 Summary and Conclusions

A second moment model for variable density and compressible flows of miscible fluids was improved by separating the transport length scale from the decay length scale. The two-length scale model demonstrates considerable improvements relative to prior single-length scale models, as shown by the significantly better matches to DNS and experimental data for a diverse array of flows. With the two-length scale model, we have demonstrated reasonable matches for statistical quantities and growth rates for homogeneous Rayleigh-Taylor turbulence, variable density Rayleigh-Taylor turbulence, homogenous shear, free shear turbulence, homogeneous isotropic turbulence decay and shocked isotropic turbulence, for which the model was calibrated. Although previous models have also shown to match variable density and shear induced turbulence, they either a) had to change coefficients for a good match, or b) could not simultaneously match growth rates and the magnitudes of the statistics. The two-length scale model significantly overcomes these shortcomings, and when compared to previous studies, shows an improvement over the single-length scale models for the range of turbulent flows considered here.

To better understand the predictive nature of the two-length scale model, we compared the model to variable density shear flow (recently obtained from DNS) and experimental shock tube data. The turbulence statistics and mean velocity shift from the model show to compare reasonably well with DNS for variable density shear flow. In addition, the comparison to shock tube data using a 1D model is also reasonable after re-shock.

Although the comparisons with homogeneous and free flows are not exact, the two-length scale model shows to be an improvement over single length scale models. Unlike previous single-length scale models, the two-length scale model is a first step towards bridging the gap between homogenous and inhomogeneous flows within the context of RANS modeling.

Acknowledgments The authors would like to thank the reviewers for constructive comments that led to an improved manuscript. They would also like to thank T. T. Clark for fruitful discussions on this subject and R. M. Rauenzahn for his help with implementing this model into the Eulerian hydrocode used for model calculations. This work was supported by the U.S. Department of Energy, subcontract #DE-AC52-06NA25396.

References

1. Cebeci, T., Smith, A.M.O.: Analysis of turbulent boundary layers, Series: Applied Mathematics and Mechanics. Academic Press, NY (1974)
2. Besnard, D., Harlow, F.H., Rauenzahn, R.M., Zemach, C.: Turbulence transport equations for variable-density turbulence and their relationship to two-field models, Los Alamos National Laboratory Technical Report, LA-UR-12303 (1992)
3. Grégoire, O., Souffland, D., Gauthier, S.: A second-order turbulence model for gaseous mixtures induced by Richtmyer-Meshkov instability. J. Turb. **6**, 1 (2005)
4. Poggi, F., Thorembey, M.-H., Rodriguez, G.: Velocity measurements in turbulent gaseous mixtures induced by Richtmyer-Meshkov instability. Phys. Fluids **10**, 2698 (1998)
5. Andronov, V.A., Barkhrakh, S.M., Meshkov, E.E., Nikiforov, V.V., Pevnitskii, A.V., Tolshmyakov, A.I.: An experimental investigation and numerical modeling of turbulent mixing in one-dimensional flows. Sov. Phys. Dokl. **27**, 393 (1982)
6. Banerjee, A., Gore, R.A., Andrews, M.J.: Development and validation of a turbulent-mix model for variable-density and compressible flows. Phys. Rev. E **82**, 046309 (2010)
7. Stalsberg-Zarling, K., Gore, R.A.: The BHR2 turbulence model: incompressible isotropic decay, Rayleigh-Taylor, Kelvin-Helmholtz and homogeneous variable density turbulence, Los Alamos National Laboratory Technical Report., LA-UR 11–04773 (2011)
8. Schwarzkopf, J.D., Livescu, D., Gore, R.A., Rauenzahn, R.M., Ristorcelli, J.R.: Application of a second-moment closure model to mixing processes involving multicomponent miscible fluids. J. Turb. **12**(49), 1 (2011)
9. Livescu, D., Ristorcelli, J.R., Gore, R.A., Dean, S.H., Cabot, W.H., Cook, A.W.: High-Reynolds number Rayleigh-Taylor turbulence. J. Turb. **10**, 1 (2009)
10. Souffland, D., Grégoire, O., Gauthier, S., Schiestel, R.: A two-time-scale model for turbulent mixing flows induced by Rayleigh-Taylor and Richtmyer-Meshkov instabilities. J. Flow Turb. Comb. **69**, 123 (2002)
11. Scheistel, R.: Multiple-time-scale modeling of turbulent flows in one-point closures. Phys. Fluids **30**(3), 722 (1987)
12. Taylor, G.I.: Diffusion by continuous movements. Proc. Lond. Math. Soc. **20**, 196 (1921)
13. Batchelor, G.K.: Diffusion in a field of homogeneous turbulence: 1. Eulerian analysis. Aust, J. Sci. Res. **2**(4), 437 (1949)
14. Tennekes, H., Lumley, J.L.: A first course in turbulence. MIT Press, MA, Cambridge (1972)
15. Frisch: Turbulence. Cambridge University Press (1995)
16. Sreenivasan, K.R.: An update on the energy dissipation rate in isotropic turbulence. Phys. Fluids **10**(2), 528 (1998)
17. Batchelor, G.K.: The theory of homogeneous turbulence. Cambridge University Press (1953)
18. Monin, A.S., Yaglom, A.M.: Statistical fluid mechanics; mechanics of turbulence. MIT Press, Cambridge, MA (1971)
19. Pope, S.B.: Turbulent Flows. Cambridge University Press, NY (2000)
20. Williams, F.A. Combustion Theory, 2nd. Addison-Wesley, Reading, MA (1985)
21. Cook, A.W.: Enthalpy diffusion in multicomponent flows. Phys. Fluids **21**, 055109 (2009)
22. Banerjee, S., Ertunç, Ö., Köksoy, Ç., Durst, F.: Pressure strain rate modeling of homogeneous axisymmetric turbulence. J. Turb. **10**, 1 (2009)
23. Gittings, M., Weaver, R., Clover, M., Betlach, T., Byrne, N., Coker, R., Dendy, E., Hueckstaedt, R., New, K., Oakes, W.R., Ranta, D., Stefan, R.: The RAGE radiation-hydrodynamic code. Comp. Sci. Disc. **1**, 015005 (2008)
24. Young, D.P., Melvin, R.G., Bieterman, M.B., Johnson, F.T., Samant, S.S., Bussoletti, J.E.: A locally refined rectangular grid finite element method: application to computational fluid dynamics and computational physics. J. Comput. Phys. **92**, 1 (1991)
25. Hanjalic, K., Launder, B.E.: A Reynolds stress model of turbulence and its application to thin shear flows. J. Fluid Mech. **52**, 609 (1972)
26. Batchelor, G.K., Townsend, A.A.: Decay of isotropic turbulence in the initial period. Proc. Roy. Soc. A **193**, 539 (1948)
27. Launder, B.E., Reese, G.J., Rodi, W.: Progress in the development of a Reynolds-stress turbulence closure. J. Fluid Mech. **68**, 537 (1975)
28. Shih, T.-S., Liou, W.W., Shabbir, A., Yang, Z., Zhu, J.: A new $k - \varepsilon$ eddy viscosity model for high Reynolds number turbulent flows. Comput. Fluid. **24**, 227 (1995)

29. King, A.T., Tinoco, R.O., Cowen, E.A.: A $k-\varepsilon$ turbulence model based on the scales of vertical shear and stem wakes valid for emergent and submerged vegetated flows. J. Fluid Mech. **701**, 1 (2012)
30. Edeling, W.N., Cinnella, P., Dwight, R.P., Bijl, H.: Baysian estimates of parameter variability in the $k-\varepsilon$ turbulence model. J. Comp. Phys. **258**, 73 (2014)
31. Mohamed, M.S., LaRue, J.C.: The decay power law in grid-generated turbulence. J. Fluid Mech. **219**, 195 (1990)
32. Perot, J.B., De Bruyn Kops, S.M.: Modeling turbulent dissipation at low and moderate Reynolds numbers. J. Turb. **7**(69) (2006)
33. Sandoval, D.L.: The dynamics of variable density turbulence, Los Alamos National Laboratory, Technical Report., LA-13037-T (1995)
34. Livescu, D., Ristorcelli, J.R.: Buoyancy-driven variable-density turbulence. J. Fluid Mech. **591**, 43 (2007)
35. Livescu, D., Ristorcelli, J.R.: Variable-density mixing in buoyancy-driven turbulence. J. Fluid Mech. **605**, 145 (2008)
36. Livescu, D., Canada, C., Burns, R.: IDIES staff, J. Pulido, 2014, Homogeneous Buoyancy Driven Turbulence Data Set, Los Alamos National Laboratory Technical Report. LA-UR-14-20669, available at http://turbulence.pha.jhu.edu/docs/README-HBDT.pdf
37. Tavoularis, S., Corrsin, S.: Experiments in nearly homogeneous turbulent shear flow with a uniform temperature gradient, Part 1. J. Fluid Mech. **104**, 311 (1981)
38. Rogers, M.M., Moin, P.: The structure of the vorticity field in homogeneous turbulent flows. J. Fluid Mech. **176**, 33 (1987)
39. Bernard, P.S., Wallace, J.M.: Turbulent Flow Analysis, Measurement and Prediction. Wiley, NJ (2002)
40. Chen, C.J., Jaw, S.Y.: Fundamentals of Turbulence Modeling. Taylor and Francis, Washington DC (1998)
41. Marusic, I., Monty, J.P., Hultmark, M., Smits, A.J.: On the logarithmic region in wall turbulence. J. Fluid Mech. **716**, R3 (2013)
42. Cabot, W.H., Cook, A.W.: Reynolds number effects on Rayleigh-Taylor instability with possible implications for type-1a supernovae. Nat. Phys. **2**, 562 (2006)
43. Rotta, J.C.: Statistische theorie nichthomogener turbulenz. Z. Phys. **129**, 547 (1951). an English translation
44. Naot, D., Shavit, A., Wolfshtein, M.: Interactions between components of the turbulent velocity correlation tensor due to pressure fluctuations. Israel J. Tech. **8**, 259 (1970)
45. Launder, B.E.: Second-moment closure: present... and future? Int. J. Heat Fluid Flow **10**, 282 (1989)
46. Bell, J.H., Mehta, R.D.: Development of a two-stream mixing layer from tripped and untripped boundary layers. AIAA J. **28**, 2034 (1990)
47. Riley, J.J., Metcalfe, R.W., Orszag, S.A.: Direct numerical simulations of chemically reacting turbulent mixing layers. Phys. Fluids **29**, 406 (1986)
48. Livescu, D., Mohd-Yusof, J., Petersen, M.R., Grove, J.W.: CFDNS: A computer code for direct numerical simulation of turbulent flows, Los Alamos National Laboratory Technical Report., LA-CC-09-100 (2009)
49. Livescu, D., Ristorcelli, J.R., Petersen, M.R., Gore, R.A.: New phenomena in variable-density Rayleigh-Taylor turbulence. Phys. Scr. T **142**, 014015–1–12 (2010)
50. Livescu, D., Wei, T., Petersen, M.R.: Direct numerical simulations of Rayleigh-Taylor instability. J. Phys.: Conf. Ser. **318**, 082007 (2011)
51. Wei, T., Livescu, D.: Late-time quadratic growth in single-mode Rayleigh-Taylor instability. Phys. Rev. E **86**, 046405 (2012)
52. Zwillinger, D. Standard Mathematical Tables and Formulae, 30th. CRC Press, Boca Raton, Fl (1996)
53. Rogers, M.M., Moser, R.D.: Direct simulation of a self-similar turbulent mixing layer. Phys. Fluids **6**, 903 (1994)
54. Pantano, C., Sarkar, S.: A study of compressibility effects in the high-speed turbulent shear layer using direct simulation. J. Fluid Mech. **451**, 329 (2002)
55. Baltzer, J.R., Livescu, Schwarzkopf, J.D.: Variable density effects in mixing layers, Los Alamos National Laboratory Technical Report., LA-UR-15-20554 (2015)
56. Rogers, M.M., Moser, R.D.: The three-dimensional evolution of a plane mixing layer: the Kelvin–Helmholtz rollup. J. Fluid Mech. **243**, 183 (1992)
57. Agui, J.H., Briassulis, G., Andreopoulos, Y.: Studies of interactions of a propagating shock wave with decaying grid turbulence: velocity and vorticity fields. J. Fluid Mech. **524**, 143 (2005)
58. Barre, S., Alem, D., Bonnet, J.P.: Experimental study of a normal shock/homogeneous turbulence interaction. AIAA J. **34**(5), 968 (1996)
59. Lee, S.S., Lele, S.K., Moin, P.: Direct numerical-simulation of isotropic turbulence interacting with a weak shock-wave. J. Fluid Mech. **264**, 373 (1993)

60. Ryu, J., Livescu, D.: Turbulence characteristics behind the shock in canonical shock-vortical turbulence interaction. J. Fluid Mech. **756**, R1 (2014)
61. Livescu, D., Ryu, J.: Vorticity dynamics after the shock-turbulence interaction, Shock Waves, doi:10.1007/s00193-015-0580-5 (2015)
62. Ribner, H.S.: Convection of a pattern of vorticity through a shock wave, NACA TR-1164 (1954)
63. Moore, F.K.: Unsteady oblique interaction of a shock wave with a plane disturbance, NACA TR-1165 (1954)
64. Sinha, K., Mahesh, K., Candler, G.V.: Modeling shock unsteadiness in shock/turbulence interaction. Phys. Fluids **15**(8), 2290 (2003)
65. Richtmyer, R.D.: Taylor instability in shock acceleration of compressible fluids. Commun. Pure Appl. Math. **13**, 297 (1960)
66. Meshkov, E.E.: Instability of the interface of two gases accelerated by a shock wave. Sov. Fluid Dyn. **4**, 101 (1969)
67. Vetter, M., Sturtevant, B.: Experiments on the Richtmyer-Meshkov instability of an air/SF_6 interface. Shock Waves **4**, 247 (1995)
68. Hill, D.J., Pantano, C., Pullin, D.I.: Large-eddy simulation and multiscale modeling of a Richtmyer-Meshkov instability with reshock. J. Fluid Mech. **557**, 29 (2006)
69. Grinstein, F.F., Gowardhan, A.A., Wachtor, A.J.: Simulations of Richtmyer-Meshkov instabilities in planar shock-tube experiments. Phys. Fluids **23**, 034106 (2011)